Identification of high-spin proton configurations in ^{136}Ba and ^{137}Ba

L. Kaya,[1,*] A. Vogt,[1] P. Reiter,[1] C. Müller-Gatermann,[1] A. Gargano,[2] L. Coraggio,[2] N. Itaco,[2,3] A. Blazhev,[1] K. Arnswald,[1] D. Bazzacco,[4] B. Birkenbach,[1] A. Bracco,[5] B. Bruyneel,[6] L. Corradi,[7] F. C. L. Crespi,[5] G. de Angelis,[7] M. Droste,[1] J. Eberth,[1] E. Farnea,[4,†] E. Fioretto,[7] C. Fransen,[1] A. Gadea,[8] A. Giaz,[5] A. Görgen,[9,10,11] A. Gottardo,[7] K. Hadyńska-Klęk,[7] H. Hess,[1] R. Hetzenegger,[1] R. Hirsch,[1] P. R. John,[12] J. Jolie,[1] A. Jungclaus,[13] W. Korten,[10] S. Leoni,[5] L. Lewandowski,[1] S. Lunardi,[14,4] R. Menegazzo,[4] D. Mengoni,[14,4] C. Michelagnoli,[15] T. Mijatović,[16] G. Montagnoli,[14,4] D. Montanari,[17] D. Napoli,[7] Zs. Podolyák,[18] G. Pollarolo,[19] F. Recchia,[14,4] D. Rosiak,[1] N. Saed-Samii,[1] E. Şahin,[9] M. Siciliano,[14,7] F. Scarlassara,[14,4] M. Seidlitz,[1] P.-A. Söderström,[20] A. M. Stefanini,[7] O. Stezowski,[21] S. Szilner,[16] B. Szpak,[22] C. Ur,[4] J. J. Valiente-Dobón,[7] M. Weinert,[1] K. Wolf,[1] and K. O. Zell[1]

[1]*Institut für Kernphysik, Universität zu Köln, D-50937 Köln, Germany*
[2]*Istituto Nazionale di Fisica Nucleare, Sezione di Napoli, I-80126 Napoli, Italy*
[3]*Dipartimento di Matematica e Fisica, Università degli Studi della Campania "Luigi Vanvitelli", viale A. Lincoln 5, I-8110 Caserta, Italy*
[4]*Istituto Nazionale di Fisica Nucleare, Sezione di Padova, I-35131 Padova, Italy*
[5]*Dipartimento di Fisica, Università di Milano and INFN Sezione di Milano, I-20133 Milano, Italy*
[6]*CEA Saclay, Service de Physique Nucleaire, F-91191 Gif-sur-Yvette, France*
[7]*Istituto Nazionale di Fisica Nucleare, Laboratori Nazionali di Legnaro, I-35020 Legnaro, Italy*
[8]*Instituto de Física Corpuscular, CSIC-Universidad de Valencia, E-46071 Valencia, Spain*
[9]*Department of Physics, University of Oslo, P. O. Box 1048 Blindern, N-0316 Oslo, Norway*
[10]*Institut de Recherche sur les lois Fondamentales de l'Univers – IRFU, CEA/DSM, Centre CEA de Saclay, F-91191 Gif-sur-Yvette Cedex, France*
[11]*Lawrence Berkeley National Laboratory, Berkeley, California 94720, USA*
[12]*Institut für Kernphysik, Technische Universität Darmstadt, D-64289 Darmstadt, Germany*
[13]*Instituto de Estructura de la Materia, CSIC, Madrid, E-28006 Madrid, Spain*
[14]*Dipartimento di Fisica e Astronomia, Università di Padova, I-35131 Padova, Italy*
[15]*Institut Laue-Langevin (ILL), 38042 Grenoble Cedex 9, France*
[16]*Ruđer Bošković Institute, HR-10 002 Zagreb, Croatia*
[17]*USIAS - Universite de Strasbourg, IPHC-CNRS, F-67037 Strasbourg Cedex 2, France*
[18]*Department of Physics, University of Surrey, Guildford, Surrey GU2 7XH, United Kingdom*
[19]*Dipartimento di Fisica Teorica dell'Università di Torino and INFN, I-10125 Torino, Italy*
[20]*Extreme Light Infrastructure-Nuclear Physics (ELI-NP), 077125 Bucharest-Magurele, Romania*
[21]*Université de Lyon, Université Lyon-1, CNRS/IN2P3, UMR5822, IPNL, F-69622 Villeurbanne Cedex, France*
[22]*Henryk Niewodniczański Institute of Nuclear Physics PAN, PL-31342 Kraków, Poland*

(Received 30 October 2018; published 2 January 2019)

The high-spin structures of ^{136}Ba and ^{137}Ba are investigated after multinucleon-transfer (MNT) and fusion-evaporation reactions. ^{136}Ba is populated in a ^{136}Xe + ^{238}U MNT reaction employing the high-resolution Advanced GAmma Tracking Array (AGATA) coupled to the magnetic spectrometer PRISMA at the Laboratori Nazionali di Legnaro, Italy, and in two ^{9}Be + ^{130}Te fusion-evaporation reactions using the High-efficiency Observatory for γ-Ray Unique Spectroscopy (HORUS) at the FN tandem accelerator of the University of Cologne, Germany. Furthermore, both isotopes are populated in an elusive reaction channel in the ^{11}B + ^{130}Te fusion-evaporation reaction utilizing the HORUS γ-ray array. The level scheme above the $J^{\pi} = 10^{+}$ isomer in ^{136}Ba is revised and extended up to an excitation energy of approximately 5.5 MeV. From the results of angular-correlation measurements, the $E_x = 3707$- and $E_x = 4920$-keV states are identified as the bandheads of positive- and negative-parity cascades. While the high-spin regimes of both ^{132}Te and ^{134}Xe are characterized by high-energy $12^{+} \rightarrow 10^{+}$ transitions, the ^{136}Ba $E2$ ground-state band is interrupted by negative-parity states only a few hundred keV above the $J^{\pi} = 10^{+}$ isomer. Furthermore, spins are established for several hitherto unassigned high-spin states in ^{137}Ba. The new results close a gap along the high-spin structure of $N < 82$ Ba isotopes. Experimental results are compared to large-scale shell-model calculations employing the GCN50:82,

*Corresponding author: levent.kaya@ikp.uni-koeln.de
†Deceased.

Realistic SM, PQM130, and SN100PN interactions. The calculations suggest that the bandheads of the positive-parity bands in both isotopes are predominantly of proton character.

DOI: 10.1103/PhysRevC.99.014301

I. INTRODUCTION

The $50 \leqslant Z,\ N \leqslant 82$ nuclei outside the doubly magic nucleus ^{132}Sn are described within the valence space made up by the orbitals $0g_{7/2}$, $1d_{5/2}$, $1d_{3/2}$, $2s_{1/2}$, and $0h_{11/2}$. $A \approx 135$ nuclei near the $N = 82$ shell closure have the Fermi surface in the middle of the proton $d_{5/2}$-$g_{7/2}$ subshell between $Z = 50$ and $Z = 64$ and offer a fertile region to deepen the understanding of the single-particle structure in the framework of the nuclear shell model and to study the evolution of different multiquasiparticle configurations formed by a combined contribution of neutron holes and proton particles.

This work focuses on the high-spin structures of ^{136}Ba and ^{137}Ba with one and two valence neutron holes outside the $N = 82$ closed shell. Isomeric yrast $J^\pi = 10^+$ states accumulate in moderately neutron-rich Xe and Ba isotopes, as well as throughout the $N = 78$, $N = 80$, and $N = 82$ isotones above the $Z = 50$ shell closure. Along the $N = 80$ isotones, between ^{130}Sn and ^{142}Sm, these isomers are predominantly of $\nu h_{11/2}^{-2}$ character and seniority $v = 2$ [1–6]. The single-particle excitation energy of the $\nu h_{11/2}$ neutron orbital is observed to increase with proton number. This increase in single-particle energy is responsible for an increase of more than 1 MeV in the excitation energy of the yrast $J^\pi = 10^+$ state between ^{130}Sn and ^{140}Nd. From the proton $Z = 64$ subshell closure at ^{144}Gd onwards, $J^\pi = 10^+$ isomers are proposed to have two-proton $\pi h_{11/2}^2$ configurations [6,7]. A compilation of high-spin level schemes above the isomeric $J^\pi = 10^+$ states along $N = 80$ is presented in Fig. 1(a).

The $10^+ \rightarrow 8^+$ isomeric transitions of ^{132}Te and ^{134}Xe have low energies of 22 and 28 keV, respectively [2]. High-spin states in the $N = 80$ isotone ^{132}Te were investigated up to spin $J^\pi = (17^+)$ with an excitation energy of 6.17 MeV [8]. The states along the $(16^+) \rightarrow (15^+) \rightarrow (14^+) \rightarrow (12^+) \rightarrow (10^+)$ cascade above the $J^\pi = 10^+$ isomer are predominantly of $\nu h_{11/2}^{-2}$ character. In ^{134}Xe, the high-spin structure above the isomeric $J^\pi = 10^+$ is known up to spin $J^\pi = (16^+)$ at 5.83 MeV. The high-spin yrast sequence is similar to ^{132}Te, despite an additional tentatively assigned $J^\pi = 13^+$ state between the $J^\pi = 12^+$ and 14^+ levels [9]. States of higher spins built on the $J^\pi = 10^+$ isomers involve the rearrangement of the valence protons since the configuration of the neutrons is already constrained. Therefore, both ^{132}Te and ^{134}Xe are characterized by high-energy $12^+ \rightarrow 10^+$ transitions of 900 and 1323 keV, respectively.

Pioneering work on ^{136}Ba focused on low-spin states up to the $J^\pi = 8^+$ state at $E_x = 2994$ keV, investigated via Coulomb excitation [10], β-decay [11], (n, γ) reactions [12], and ^{9}Be-induced fusion-evaporation reactions [13]. The $J^\pi = 10^+$ state at $E_x = 3357$ keV with a $\nu h_{11/2}^{-2}$ configuration was simultaneously discovered by Shizuma *et al.* [14] employing a ^{82}Se + ^{139}La deep-inelastic reaction at 450 MeV and by Valiente-Dobón *et al.* [3] who populated ^{136}Ba in a ^{136}Xe + ^{198}Pt multinucleon-transfer reaction at a beam energy of 850 MeV. The groups reported half-lives of $T_{1/2} = 94(10)$ ns [14] and $T_{1/2} = 91(2)$ ns [3]. Valiente-Dobón *et al.* employed prompt-delayed correlations to identify seven γ-ray transitions feeding the $J^\pi = 10^+$ state and established a tentative high-spin structure. Contrary to ^{132}Te and ^{134}Xe, the next excited state is located only 349 keV above the 3357-keV isomeric state. According to shell-model calculations and systematics, it was assumed that the excitation pattern above the $J^\pi = 10^+$ state does not correspond to an $E2$ yrast sequence. Instead, a $J^\pi = 10^-$, 11^-, or 12^- assignment was suggested for the $E_x = 3707$-keV state. However, angular-correlation measurements were not in the scope of the experiment [3].

Approaching the proton subshell closure, elaborate high-spin information from heavy-ion fusion-evaporation reactions are available for both ^{138}Ce and ^{140}Nd [15,16]. Measurements of the $J^\pi = 10_1^+$ isomer's g factors in both nuclei corroborated $\nu h_{11/2}^{-2}$ neutron-hole configurations [5]. In ^{138}Ce the $E2$ yrast sequence is interrupted by an intermediate $J^\pi = 11^+$ state, connecting $J = 12$ states of positive and negative parity with the 82(2)-ns $J^\pi = 10^+$ isomer. Going to higher spins, the level structure is significantly fragmented into several band structures dominated by different quasiparticle configurations [15].

The high-spin regime of ^{140}Nd is even more fragmented and explained by different two-neutron and two-proton excitations [16–18]. The 33(2)-ns $J^\pi = 10_1^+$ isomer decays via negative-parity states to the 0.6-ms $J^\pi = 7_1^-$ state. It is directly fed by $J^\pi = 11^-$ and $J^\pi = 10^-$ states [18]. A second $J^\pi = 10^+$ state was identified at 4155 keV, fed by positive-parity states [16]. Furthermore, ^{140}Nd exhibits a six-quasiparticle $J^\pi = 20^+$ isomer with a half-life of $T_{1/2} = 1.23(7)\ \mu$s at 7430 keV [19].

Similar to the $J^\pi = 10^+$ isomers along $N = 80$, $J^\pi = 19/2^-$ isomers are a common feature of nuclei along $N = 81$ [4,20,21]. A compilation of several partial level schemes above the $J^\pi = 19/2^-$ isomers is shown in Fig. 1(b).

The level scheme of ^{133}Te is known up to 6.2 MeV with tentative spin assignments up to $J^\pi = (31/2^-)$ [24,25]. A $J^\pi = (19/2^-)$ state at 1.610 MeV is found to be isomeric with an adopted half-life of $T_{1/2} = 100(5)$ ns [26]. In ^{135}Xe the high-spin regime is investigated up to 4.07 MeV, however, no spin and parities are known beyond the $J^\pi = 19/2^-$ state which is identified as an isomer with a half-life of $T_{1/2} = 9.0(9)$ ns [20].

Pioneering studies of ^{137}Ba mainly focused on low- and medium-spin states. Data were obtained utilizing β decay [27,28], neutron-induced reactions [29], and Coulomb excitation [30]. The spins, parities, and half-lives of the ground state and the $J^\pi = 11/2^-$ isomer at 661.659(3) keV with a half-life of 2.552(1) min are well established. First results on medium-spin states of ^{137}Ba were obtained by Kerek *et al.*

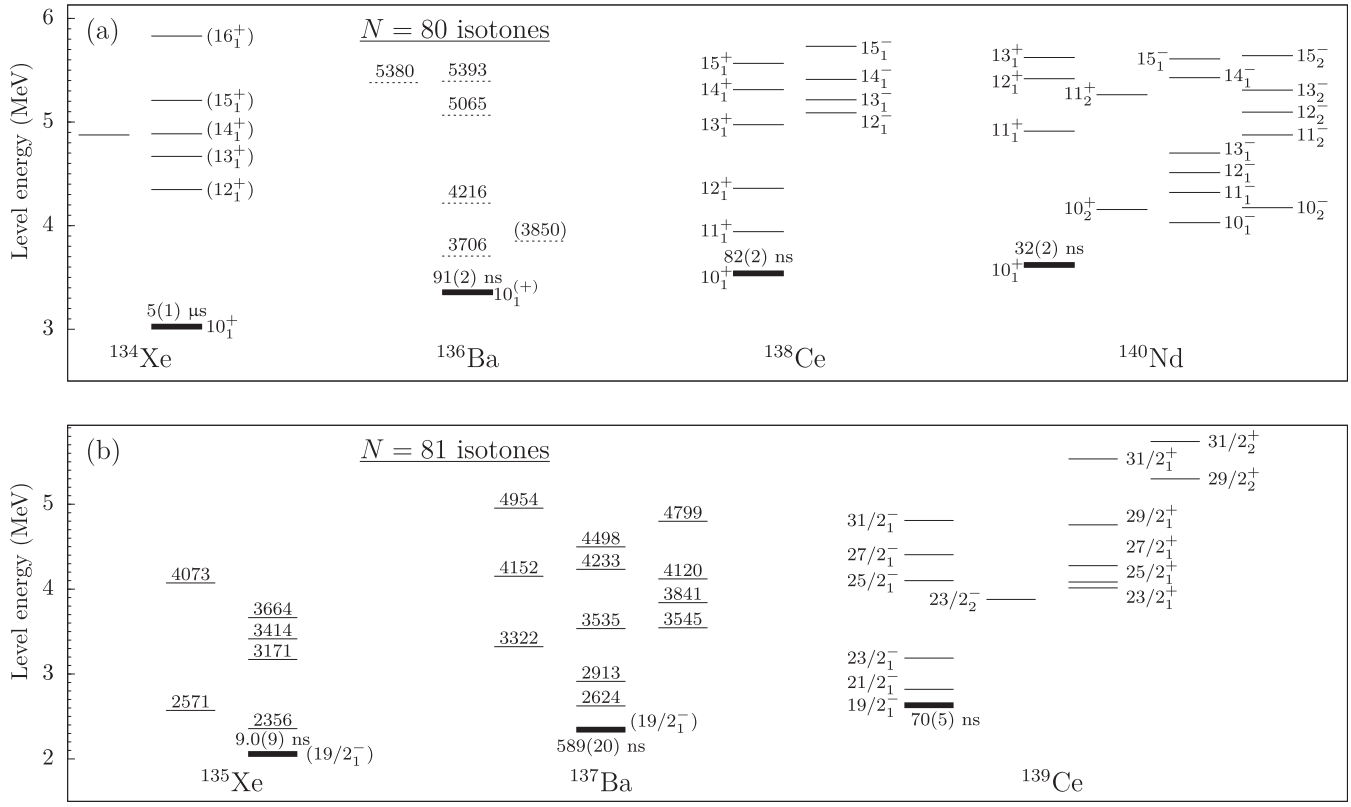

FIG. 1. Comparison of high-spin states above (a) the $J^\pi = 10^+_1$ isomers along $N = 80$ and (b) above the $J^\pi = 19/2^-_1$ isomers along $N = 81$. There is a significant lack of information on spin assignments in ^{136}Ba and ^{137}Ba. Data taken from Refs. [3,9,15,16,18,20–23].

in 1973 [21], via an α-induced reaction on a ^{136}Xe-enriched gas target. An isomeric state at $E_x = 2350$ keV with possible spin assignments $J^\pi = (15/2, 17/2, 19/2)$ and a half-life of $T_{1/2} = 590(100)$ ns was observed. This state was found to decay via a 120-1568-keV γ-ray cascade, finally populating the long-lived $J^\pi = 11/2^-_1$ isomer. The authors of the present work studied ^{137}Ba as a multinucleon-transfer and fusion-evaporation product using the Advanced Gamma-ray Tracking Array (AGATA) + PRISMA setup at LNL Legnaro, the GAMMASPHERE array at Lawrence Berkeley National Laboratory and the HORUS array at Cologne [20]. The level scheme was extended up to approximately 5 MeV excitation energy. Spin and parity assignments of high-spin states were not subjects of the work [20].

In ^{139}Ce the yrast negative-parity band based on the $J^\pi = 19/2^-$ isomer is well established up to an excitation energy of approximately 8 MeV [31,32]. A band on top of a $J^\pi = 19/2^-$ isomer was initially proposed to be of negative parity [31,32]. Recently, this structure was revised to be a positive-parity cascade built on top of a $J^\pi = 23/2^+$ bandhead decaying into the $J^\pi = 19/2^-$ isomer [23].

Adding two more protons, a plethora of high-spin bands were discovered in ^{141}Nd [33,34]. In an earlier experiment [4], delayed time distributions indicated a possible $J = 19/2^-$ isomeric state with $T_{1/2} = 26(5)$ ns at an energy of $2886 + x$ keV. However, this isomer was not confirmed by subsequent studies [33,34]. Moreover, no evidence of a positive-parity band connected to the $J^\pi = 19/2^-$ isomer was found to date. Thus, the typical features of $J^\pi = 19/2^-$ isomers and the associated feeding high-spin structures along $N = 81$ could be first discontinued in ^{141}Nd.

Along the $N = 80$ and $N = 81$ isotones, spin and parity assignments are missing inter alia for ^{136}Ba and ^{137}Ba. Available information is limited to in part tentative excitation energies. The aim of the present work is to complement these earlier studies with spin and parity assignments of the high-spin states. The systematics along the $N = 80$ chain suggest that the yrast $E2\,12^+ \rightarrow 10^+$ cascades are first interrupted in ^{136}Ba accompanied by a change in nuclear structure. This motivates a refined investigation of the high-spin features above the isomeric $J^\pi = 10^+$ state in ^{136}Ba and above the isomeric $J^\pi = 19/2^-$ state in ^{137}Ba.

In this paper new results on ^{136}Ba and ^{137}Ba are presented. ^{136}Ba was populated in a ^{136}Xe + ^{238}U multinucleon-transfer (MNT) experiment employing the AGATA γ-ray spectrometer [35] in combination with the magnetic mass spectrometer PRISMA [36–38]. Moreover, ^{136}Ba is investigated in two ^{9}Be + ^{130}Te and one ^{11}B + ^{130}Te fusion-evaporation experiment employing two different configurations of the High-efficiency Observatory for γ-Ray Unique Spectroscopy (HORUS) [39] at the Institute of Nuclear Physics, University of Cologne. ^{137}Ba was populated in the ^{11}B + ^{130}Te fusion-evaporation experiment. The HORUS experiments provide detailed information on $\gamma\gamma$ coincidences and angular correlations.

This paper is organized as follows: the experimental setup and data analysis of the experiments are described in Sec. II, followed by the experimental results in Sec. III. A

comparison with large-scale shell-model calculations is presented in Sec. IV before the paper is completed with a summary and conclusions.

II. EXPERIMENTAL PROCEDURE

A. ^{136}Xe + ^{238}U multinucleon transfer

In this experiment, ^{136}Ba was populated in a ^{136}Xe + ^{238}U multinucleon-transfer experiment at the Laboratori Nazionali di Legnaro, Italy. The 6.84 MeV/nucleon ^{136}Xe beam, accelerated by the PIAVE+ALPI accelerator complex, impinged onto a 1- and a 2-mg/cm^2 ^{238}U target. An isotopic identification of the nuclei of interest was provided by the magnetic spectrometer PRISMA placed at the reaction's grazing angle of $\theta_{\rm lab} = 50^\circ$. γ rays from excited states in both beam- and targetlike nuclei were detected with the AGATA γ-ray spectrometer [35] in the demonstrator configuration [40] placed 23.5 cm from the target position. The array consisted of 15 large-volume electronically segmented high-purity Ge (HPGe) detectors in five triple cryostats [41]. An event registered by the PRISMA focal-plane detector in coincidence with an AGATA event was taken as a trigger for the data acquisition. In this way the origin of the γ rays is distinguished, background from beta decay is reduced, and a major fraction of isomeric γ-ray transitions is suppressed.

Pulse-shape analysis of the digitized detector signals was applied to determine the individual interaction points within the HPGe shell [42], enabling the Orsay forward-tracking algorithm [43] to reconstruct the individual emitted γ-ray energies, determine the first interaction point of the γ ray in the germanium, and, thus, the emission angle. Together with the kinematic information from PRISMA, a precise Doppler correction was performed. Further details on the analysis can be found in Ref. [44].

B. Part I: ^{9}Be + ^{130}Te fusion-evaporation reaction

In this experiment excited states in ^{136}Ba were populated in a ^{9}Be + ^{130}Te fusion-evaporation reaction. The FN Tandem accelerator of the Institute of Nuclear Physics, University of Cologne, provided a 40-MeV ^{9}Be beam. In this and two additional experiments, introduced in Secs. II B–II D, the target consisted of 99.3% enriched ^{130}Te with a thickness of 1.8 mg/cm^2, evaporated onto a 120-mg/cm^2-thick Bi backing plus a 132-mg/cm^2-thick Cu layer for heat dissipation. In the three experiments, all reaction products were stopped inside the Bi backing. γ rays from excited reaction products were measured with a γ-ray array equipped with 11 high-purity germanium (HPGe) detectors, placed in rings at 45° (six detectors) and 143° (five detectors) with respect to the beam axis. In total, 9×10^7 $\gamma\gamma$-coincidence events were collected.

C. Part II: ^{9}Be + ^{130}Te fusion-evaporation reaction

Another ^{9}Be + ^{130}Te fusion-evaporation reaction was performed at 43 MeV beam energy. The HORUS array comprised 14 HPGe detectors, six of them equipped with BGO Compton-suppression shields. The detectors were positioned on the eight corners and six faces of a cube. To reduce background radiation from x rays, each detector was shielded by 2-mm-thick sheets of lead and copper. Note that the relative efficiency of the first experiment (Sec. II B) exceeds the relative efficiency of the second experiment by a factor of more than 16 at a γ-ray energy of 100 keV. However, the total $\gamma\gamma$ statistic is more than one order of magnitude higher than in the first experiment.

D. ^{11}B + ^{130}Te fusion-evaporation reaction

In the third experiment, ^{136}Ba and ^{137}Ba were populated via a ^{11}B + ^{130}Te fusion-evaporation reaction. Several fusion-evaporation codes predict a relative cross section of $<1\%$ for the evaporation channels of interest. The HORUS array was arranged similarly to the second ^{136}Ba experiment (Sec. II C). However, no additional shielding in front of the detectors was mounted. In total, 1.5×10^{10} $\gamma\gamma$-coincidence events were recorded. Additional information about the experimental setup and the results of the $\gamma\gamma$ analysis of this experiment can be found in Ref. [20].

In all three fusion-evaporation experiments, γ-ray events were processed triggerless and recorded utilizing the synchronized 80-MHz XIA$^{\rm TM}$Digital Gamma Finder (DGF) data-acquisition system. The data were analyzed offline using the codes SOCO-V2 [45] and TV [46].

The HORUS spectrometer arranged in the cube configuration allows us to investigate multipole-mixing ratios of transitions between excited states with the $\gamma\gamma$ angular-correlation code CORLEONE [47,48] based on the phase convention by Krane, Steffen, and Wheeler [49,50]. Different hypotheses of involved spins J_1, J_2, J_3 and multipole-mixing ratios δ_1, δ_2 of two coincident γ rays in a cascade $J_1 \xrightarrow{\delta_1} J_2 \xrightarrow{\delta_2} J_3$ are evaluated by χ^2 fits of the correlation function $W(\Theta_1, \Theta_2, \Phi) = W(J_1, \delta_1, J_2, \delta_2, J_3)$ to experimental intensities in eight different correlation groups, each associated with detector pairs at angles $\Theta_{1,2}$ with respect to the beam axis and a relative angle Φ between the planes spanned by the detectors and the beam axis. Note that the correlation intensities also depend on the orientation parameter σ: the fusion-evaporation reaction orients the spin of the initial level J_1 with respect to the beam axis. The orientation is described by a Gaussian distribution of the magnetic substates with mean value $\langle m \rangle = 0$ and variance σ^2. The width of the alignment distribution was found to be constant at $\sigma = 2.1$. More details on the angular-correlation analysis with CORLEONE are given in Refs. [51,52]

III. EXPERIMENTAL RESULTS

A. ^{136}Ba

The level scheme of ^{136}Ba deduced in the four experiments is presented in Fig. 2(a). New parity assignments of states above the $J^\pi = 10^+$ isomer are based on the parity assignments of the isomeric 3357-keV state in ^{136}Ba given in Refs. [3,14]. The $J^\pi = 10^+$ assignment with the tentative positive parity is strongly supported by systematics, shell-model calculations, and measured DCO ratios [3,14].

The Doppler-corrected AGATA singles γ-ray spectrum of ^{136}Ba in the ^{136}Xe + ^{238}U experiment is shown in Fig. 3(a). The mass spectrum along the Ba isotopes identified with

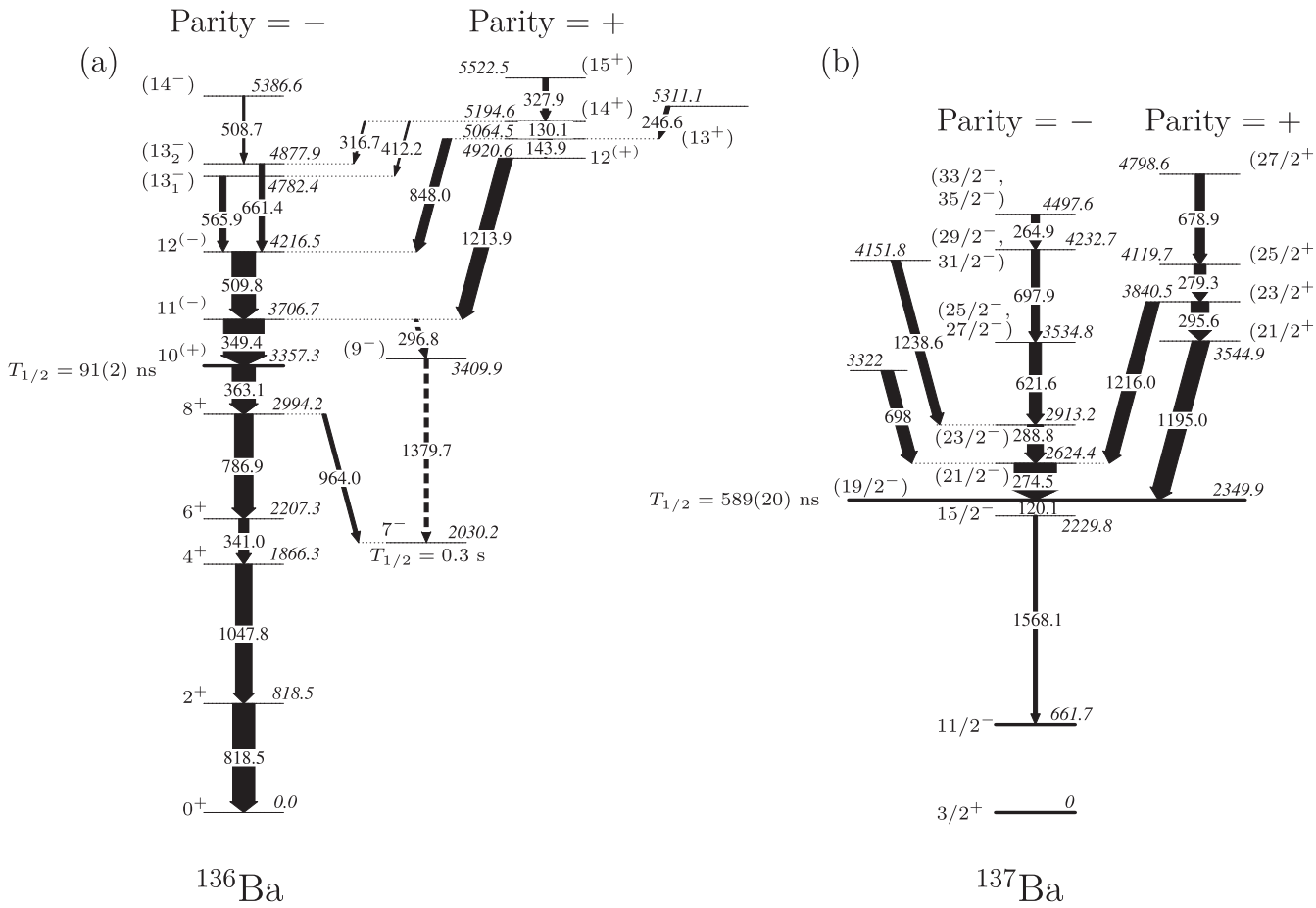

FIG. 2. (a) Level scheme assigned to ^{136}Ba in the present work. Transitions and excitation energies are given in keV. γ-ray intensities above the $J^{\pi} = 10^{+}$ isomer are deduced from the ^{9}Be + ^{130}Te experiment and normalized to the 349-keV transition. (b) Level scheme assigned to ^{137}Ba and normalized to the 275-keV transition. Transitions and excitation energies are taken from the previous work, using the same ^{11}B + ^{130}Te experiment, presented in Ref. [20]. Tentative assignments are given in brackets and dashed lines. In both isotopes new spin/parity assignments are based on the spin/parity assignments of the isomeric 3357.3-keV state in ^{136}Ba given in Ref. [14] and on the spin/parity assignments of the isomeric 2349.9-keV state in ^{137}Ba given in Refs. [20,21]. See text for details.

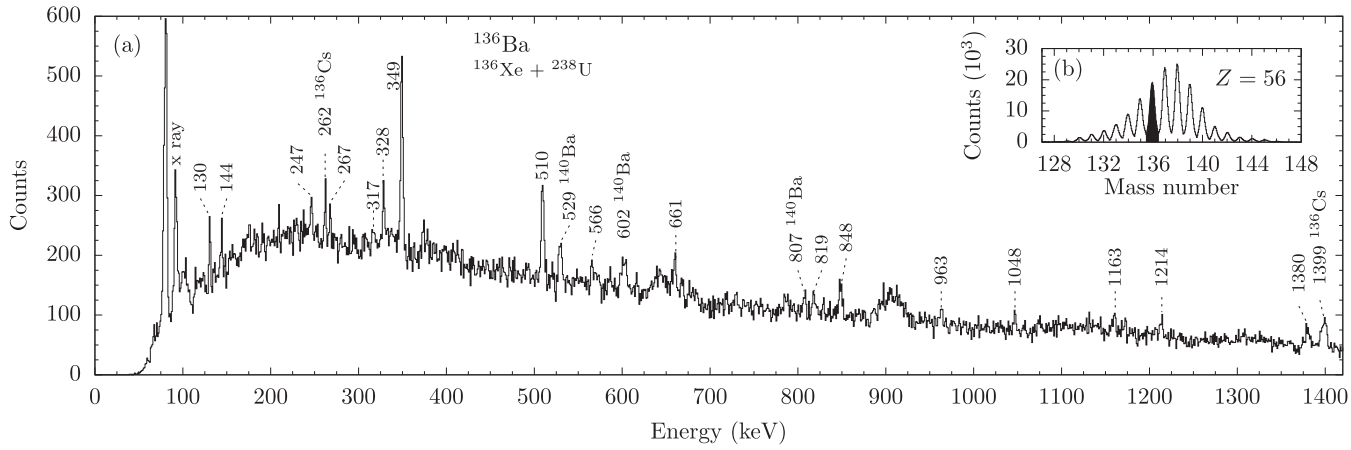

FIG. 3. (a) Doppler-corrected γ-ray spectrum gated on ^{136}Ba identified in PRISMA in the ^{136}Xe + ^{238}U experiment. γ-ray energies are given in keV. (b) Mass spectrum of Ba isotopes identified with PRISMA. The applied mass gate on ^{136}Ba is marked black. A gate on the prompt time peak between AGATA and PRISMA is applied to reduce random background.

TABLE I. Energies, spin assignments, and relative in-beam intensities for γ-ray transitions in ^{136}Ba above the $J^\pi = 10^+_1$ isomer at $E_x = 3357.3$ keV. Fitted energies and relative intensities normalized to the 349.4-keV transition are taken from two experiments: $I_\gamma^{^{11}\mathrm{B}}$ from $^{11}\mathrm{B} + {}^{130}\mathrm{Te}$ and $I_\gamma^{^{9}\mathrm{Be}}$ from $^{9}\mathrm{Be} + {}^{130}\mathrm{Te}$.

E_γ (keV)	E_i (keV)	E_f (keV)	I_i^π	I_f^π	$I_\gamma^{^{11}\mathrm{B}}$	$I_\gamma^{^{9}\mathrm{Be}}$
130.1	5194.6	5064.5	(14^+)	(13^+)	20(2)	18(2)
143.9	5064.5	4920.6	(13^+)	$12^{(+)}$	29(2)	23(2)
296.8	3706.7	3409.9	$11^{(-)}$	(9^-)	–	weak
316.7	5194.6	4877.9	(14^+)	(13^-_2)	9(2)	weak
246.6	5311.1	5064.5	–	(13^+)	12(3)	10(1)
327.9	5522.5	5194.6	(15^+)	(14^+)	12(3)	13(2)
349.4	3706.7	3357.3	$11^{(-)}$	$10^{(+)}$	≡100	≡100
412.2	5194.6	4782.4	(14^+)	(13^-_1)	10(2)	weak
508.7	5386.6	4877.9	(14^-)	(13^-_2)	weak	weak
509.8	4216.5	3706.7	$12^{(-)}$	$11^{(-)}$	62(9)	63(7)
565.9	4782.4	4216.5	(13^-_1)	$12^{(-)}$	25(3)	15(1)
661.4	4877.9	4216.5	(13^-_2)	$12^{(-)}$	20(2)	13(1)
848.0	5064.5	4216.5	(13^+)	$12^{(-)}$	30(3)	27(3)
1213.9	4920.6	3706.7	$12^{(+)}$	$11^{(-)}$	42(4)	35(3)
1379.7	3409.9	2030.2	(9^-)	7^-	–	weak

PRISMA and the applied gate on ^{136}Ba is shown in the inset Fig. 3(b). Transitions at γ-ray energies of 529, 602, and 807 keV are contaminants from the $+4n$ channel ^{140}Ba. Moderately weak lines at 262 and 1399 keV can be associated to known transitions in the isobar ^{136}Cs. Due to the restriction to prompt events in the time-difference spectrum between PRISMA and AGATA, i.e., $\Delta t_{\mathrm{PRISMA\text{-}AGATA}} \approx 16$ ns, transitions between states below the $E_x = 3357$ keV, $J^\pi = 10^+$ isomer are found to be suppressed in the spectrum. The largest peaks in the spectrum are located at 349 and 510 keV. In previous works both transitions were placed on top of the 3357-keV isomer to form a cascade deexciting the 4217-keV state [3,14]. Further peaks at 130, 144, 247, 328, 848, and 1214 keV are consistent with those found by Valiente-Dobón *et al.* [3]. However, the placement of 130- and 247-keV transitions was unknown in the level scheme of the previous work due to similar relative peak intensities.

Measured intensities of coincident γ rays from the HORUS experiments are summarized in the right-hand side of Table I. All intensities are efficiency corrected and normalized to the intensity of the 349-keV transition. Intensities are extracted from the $^{9}\mathrm{Be} + {}^{130}\mathrm{Te}$ experiment ($I_\gamma^{^{9}\mathrm{Be}}$) as well as from the $^{11}\mathrm{B} + {}^{130}\mathrm{Te}$ experiment ($I_\gamma^{^{11}\mathrm{B}}$). The independently measured intensities show a consistent assignment of states and transitions. The uncertainties in the transition energies are ±0.5 keV. Spin/parity assignments are supported by angular-correlation measurements and shell-model calculations. Various HORUS background-subtracted prompt $\gamma\gamma$-coincidence spectra from the first $^{9}\mathrm{Be} + {}^{130}\mathrm{Te}$ experiment (see Sec. II B) with gates on transitions above the $J^\pi = 10^+$ isomer are shown in Figs. 4(a)–4(d). Contaminant transitions in the spectrum gated on the 328-keV transition [Fig. 4(c)] stem from $35/2^- \rightarrow 33/2^-$ transition in ^{135}Ba [53]. Coincident transitions deexciting the isomeric $E_x = 3357$-keV state are suppressed in intensity, due to the prompt $\gamma\gamma$-coincidence time gate of 175 ns.

Figure 4(a) presents the γ-ray spectrum with a gate on the 349-keV transition. Coincidences are labeled with filled arrowheads. The spectrum exhibits anticipated coincidences at 144, 328, 510, 848, and 1214 keV. Unassigned peaks at 130, 247, 566, and 661 keV, observed in the AGATA experiment, are coincident to the 349-keV transition. In the previous work [3], the 144- and 1214-keV γ rays are arranged to form a state at $E_x = 3850$ keV. A gate on the 848-keV transition is shown in Fig. 4(b). The absence of the 144-1214-keV cascade requires the 848-keV transition to be placed parallel to this cascade. The intensity of the 1214-keV peak in the $\gamma\gamma$-coincidence spectrum gated on 349 keV exceeds the one of the 144-keV line. Moreover, the 144-1214-keV cascade corresponds to the sum energy of the 848-510-keV cascade. Therefore, in accordance with the measured intensity relations of the 1214- and 144-keV transitions, the 144-keV transition has to be placed on top of the 1214-keV transition, resulting in a new state at 4921 keV excitation energy.

Coincidences with the 848-keV and 1214-keV transitions as well as intensity balances require a placement of the 130, 247, and 328-keV transitions above the 5065-keV state. Since the 130-keV transition is mutually coincident with the 328-keV transition [cf. Fig. 4(c)], both transitions form a 328-130-keV cascade on top of the $E_x = 5065$-keV state. The ordering of the 328- and 130-keV transitions agrees with the intensity balance measured in the $\gamma\gamma$ projections gated on the 144-, 349-, 848-, and 1214-keV transitions. Additionally, Fig. 4(d) shows that the 247-keV transition is not coincident with the 328-130-keV cascade. Consequently, the 247-keV transition is placed parallel to the 328-130-keV cascade to establish a state at $E_x = 5311$ keV.

Moreover, Fig. 4(a) shows two additional coincidences at 566 and 661 keV, however, both transitions are neither coincident with the transitions at 848 and 328 keV, nor with the 247-keV transition [cf. Figs. 4(a)–4(d)]. Due to insufficient statistics we use the higher $\gamma\gamma$ statistics from the second $^{9}\mathrm{Be} + {}^{130}\mathrm{Te}$ experiment (see Sec. II C) to place the 566- and 661-keV transitions in the level scheme. We remind the reader that although the total $\gamma\gamma$ statistics of this experiment is higher, the efficiency at small energies is limited due to the use of absorbers.

Figures 4(e)–4(g) show double-gated $\gamma\gamma\gamma$-coincidence and sums of double-gated $\gamma\gamma\gamma$-coincidence spectra. Both the 566- and 661-keV transitions emerge in the $\gamma\gamma\gamma$ projection gated on 510 and 349 keV, as displayed in Fig. 4(e). Hence, the transitions have to feed the 4217-keV state. Since the 566- and 661-keV transitions are not in mutual coincidence [cf. Figs. 4(f)–4(g)] both have to be placed parallel, directly feeding the $E_x = 4217$-keV state.

Furthermore, the spectrum gated on the 510-349-keV cascade [cf. Fig. 4(e)] reveals weak lines at 317 and 412 keV. The 317-keV transition corresponds to the energy difference between the new established states at 4878 and 5195 keV, while the 412-keV transition corresponds to the transition between the new established states at 4782 and 5195 keV. As expected, the 412-keV transition is only observed in coincidence with the 566-keV transition [cf. Fig. 4(f)] and

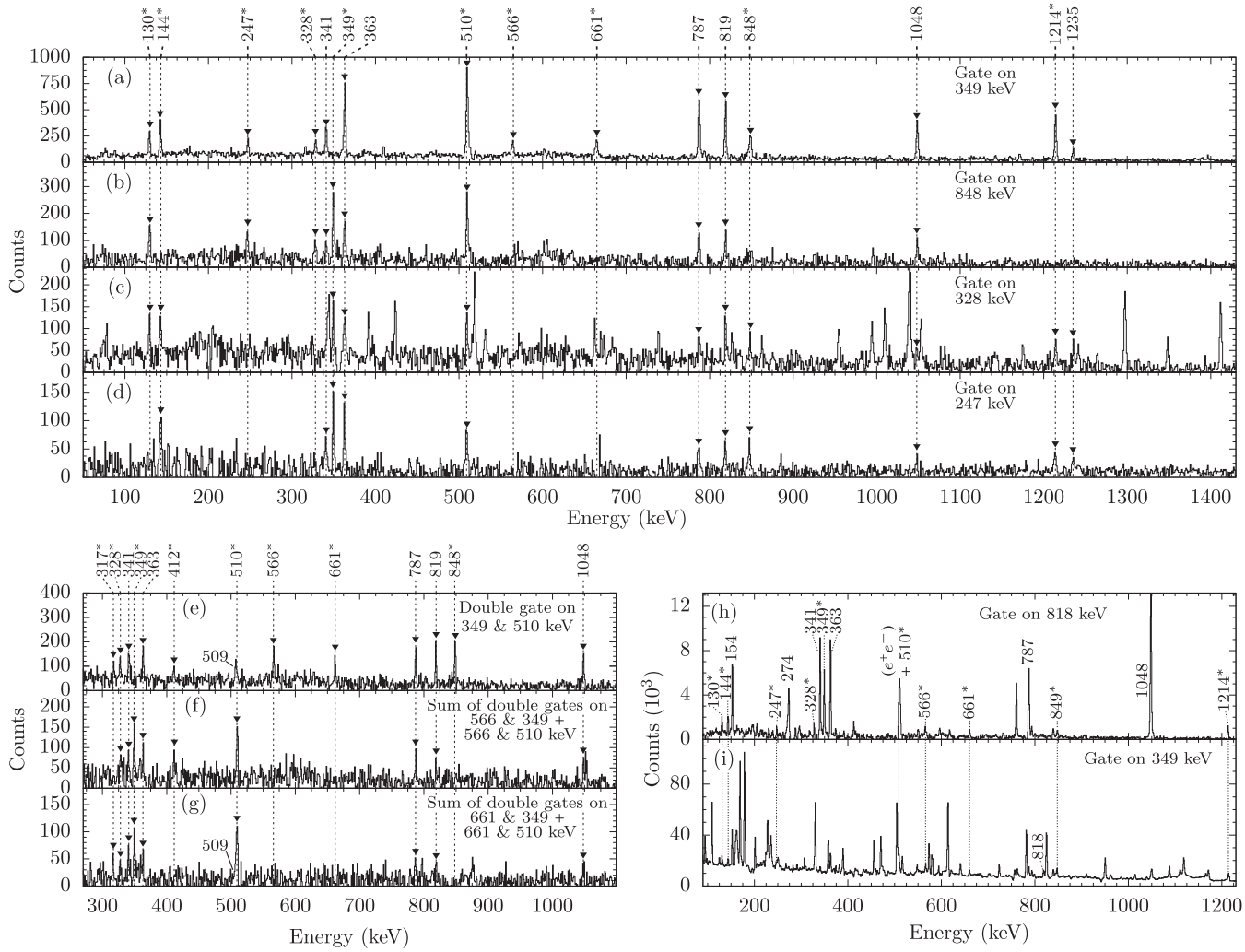

FIG. 4. Prompt $\gamma\gamma$ double-coincidence spectra from the first ^{9}Be + ^{130}Te experiment (see Sec. II B) with gates on (a) 349, (b) 848, (c) 328, and (d) 247 keV. Transitions above the $J^{\pi} = 10^{+}$ isomer are marked with asterisks. Coincidences are labeled by filled arrowheads. Contaminant transitions in the spectrum gated on the 328 keV stem from transitions in ^{135}Ba. $\gamma\gamma\gamma$ triple-coincidence spectra from the second ^{9}Be + ^{130}Te experiment (see Sec. II C) with (e) a double gate on 349 and 510 keV, a sum of double-gated triples coincidence spectra gated on (f) 566 and 510 and 566 and 349 keV, and a similar sum spectra gated on (g) 661 and 510 and 661 and 349 keV. Prompt $\gamma\gamma$ double-coincidence spectra with a gate on (h) 818 and (i) 349 keV from the ^{11}B + ^{130}Te experiment (see Sec. II D). The gate on 349 keV is contaminated with transitions from ^{137}La.

the 317-keV transition is in coincidence with the 661-keV transition [cf. Fig. 4(g)].

A further 509-keV transition is in coincidence with the 510-349-keV cascade, as shown in Fig. 4(e). The centroid of this peak is clearly separated by 0.9 keV from the 510-keV peak position in Fig. 4(f). Since the full width at half maximum (FWHM) of the coincident 510-keV transition gated on 566-keV is broader than the similar peak gated on 661 keV, the 509-keV transition is identified as another transition above the 4878-keV state.

An intense 1380-keV transition is observed in the AGATA spectrum in Fig. 3. In accordance with previous studies performed with the AGATA dataset [9,20], a transition from a contaminant can be excluded. In the HORUS experiment this transition is observed to be coincidence with transitions stemming from the $5^{-} \rightarrow 2^{+}$ decay in ^{134}Ba and in coincidence with a 297-keV transition. Assuming a 1380-keV transition above the $J^{\pi} = 7^{-}$ isomer at $E_x = 2030$ keV, the energy difference between the 3707-keV state and a proposed $E_x = 3410$ keV state corresponds to 297 keV. Accordingly, the 297-1380-keV cascade is tentatively placed above the $J^{\pi} = 7^{-}$ isomer, connecting the $E_x = 3707$-keV state with the isomer. This assignment is further supported by the recent observation of a similar 415-1099-keV cascade on top of the $J^{\pi} = 7^{-}$ isomer in the isotone ^{134}Xe [9].

^{136}Ba was also populated in the ^{11}B + ^{130}Te fusion-evaporation experiment with a significantly lower relative cross section (see Sec. II D). Figures 4(h) and 4(i) show exemplary prompt $\gamma\gamma$-coincidence spectra with gates on the 818- and 349-keV transitions. Besides dominant coincident transitions originating from the 348-keV $(33/2^{+} \rightarrow 31/2^{-})$ decay in ^{137}La [54], also transitions from ^{136}Ba, including

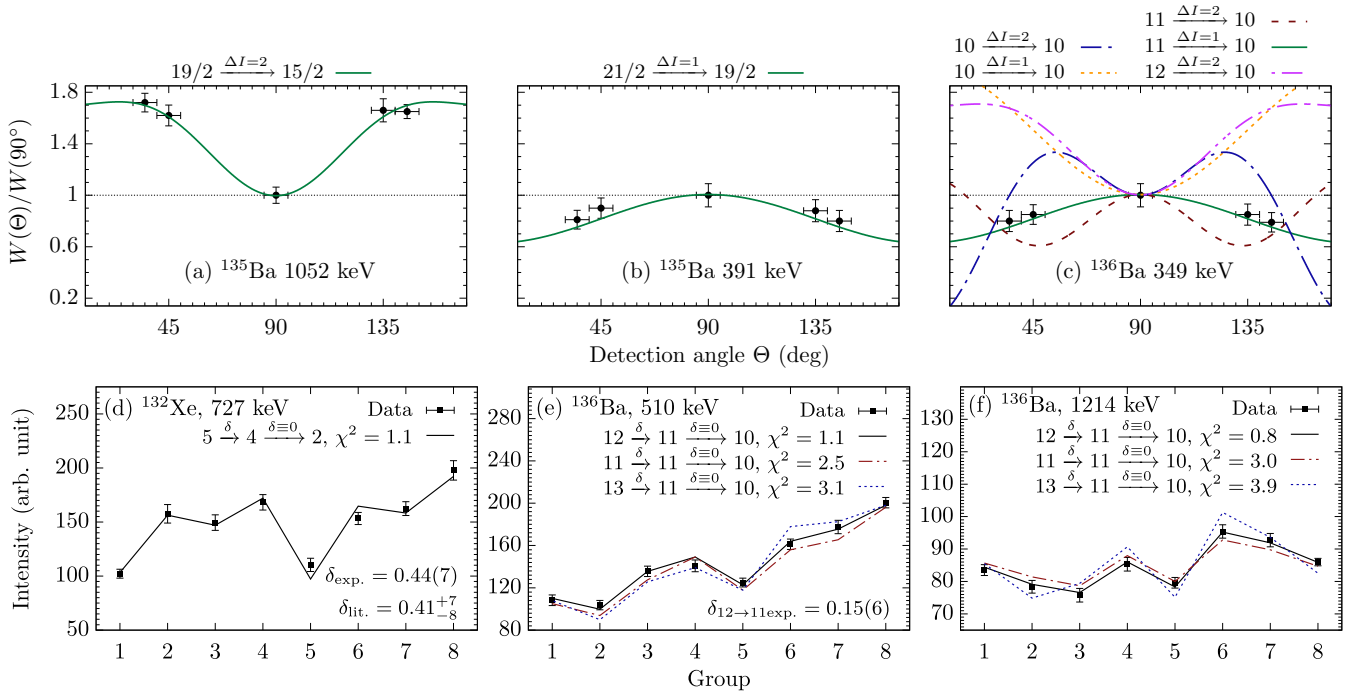

FIG. 5. Benchmark angular distribution of (a) the 1052-keV ($19/2^- \rightarrow 15/2^-$) γ-ray transition and (b) the 391-keV ($21/2^- \rightarrow 19/2^-$) γ-ray transition, both in ^{135}Ba. Experimental values (data points) are compared to pure dipole and quadrupole hypotheses (solid lines). (c) Angular distribution of the 349-keV transition, feeding the $J^\pi = 10^+$ isomer in ^{136}Ba. Several pure dipole and quadrupole hypotheses (lines) are plotted. (d) Benchmark $\gamma\gamma$ angular correlations for the $5_1^+ \rightarrow 4_1^+ \rightarrow 2_1^+$ (727-773-keV) cascade in ^{132}Xe. Experimental values (data points) are compared to calculated angular-correlation functions $W(\Theta_1, \Theta_2, \Phi)$ (lines) for eight correlation groups using the code CORLEONE. Investigation for (e) the 510-349-keV cascade and (f) the 1214-349-keV cascade in ^{136}Ba. Several spin hypotheses are plotted.

the new established transitions, are observed well above the background. Intensities ($I_\gamma^{^{11}\mathrm{B}}$), normalized to the intensity of the 349-keV transition, are listed in Table I. The observed coincidences in the $^{11}\mathrm{B} + ^{130}\mathrm{Te}$ experiment are consistent with the aforementioned results and strongly support the new results on ^{136}Ba.

The detectors in the HORUS setup of the $^{9}\mathrm{Be} + ^{130}\mathrm{Te}$ experiment (see Sec. II C) were arranged in a cube configuration, yielding five rings at relative angles of 35° (ring 1), 45° (ring 2), 90° (ring 3), 135° (ring 4), and 145° (ring 5) with respect to the beam axis. Figure 5(a) shows the distribution of the measured singles γ-ray intensity of the well-known 1052-keV transition ($19/2^- \xrightarrow{E2} 15/2^-$) in ^{135}Ba in the different rings, normalized to the intensity of ring 3. Moreover, Fig. 5(b) shows a similar distribution for the 391-keV transition ($21/2^- \xrightarrow{E1} 19/2^-$) in ^{135}Ba. Both distributions are compared with theoretical pure dipole- and quadrupole-transition hypotheses as described by Yamazaki *et al.* [55]. Both angular distributions are symmetric around 90°. The intensity of the quadrupole 1052-keV transition ($\Delta I = 2$) in Fig. 5(a) is maximum along the beam axis, whereas the one of the dipole 391-keV transition ($\Delta I = 1$) in Fig. 5(b) is maximum perpendicular to the beam axis, demonstrating spin alignment with respect to the beam axis.

The characteristic investigation of dipole and quadrupole radiation signatures in the HORUS experiment is used to determine the multipolarity of the 349-keV transition in ^{136}Ba. In Fig. 5(c) the singles γ-ray intensity distribution of the 349-keV transition is compared to different theoretical pure dipole and quadrupole distributions for spins $J = 10, 11, 12$ of the $E_x = 3707$-keV state. The $12 \xrightarrow{\Delta I=2} 10$ and $10 \xrightarrow{\Delta I=1} 10$ hypotheses can be clearly rejected. Since the 349-keV γ ray has a Weisskopf half-life estimate of $T_{1/2} = 0.17$ ms for an $E3$ transition, an $E3$ character is disregarded. Possible $10 \xrightarrow{\Delta I=2} 10$ and $11 \xrightarrow{\Delta I=2} 10$ hypotheses show large discrepancies between theoretical and experimental values. Moreover, a mixed dipole-quadrupole transition with initial spin of $J^\pi = 10^+$ does not provide a better agreement. Hence, the four above-mentioned hypotheses can be rejected. A pure dipole decay and an initial spin of $J = 11$ for the $E_x = 3707$-keV state yields the best agreement with the experimental intensity distribution.

Based on the assigned spin of the $E_x = 3707$-keV state, further spin hypotheses are tested for the $E_x = 4217$-keV and the newly established $E_x = 4921$-keV states applying the procedure of $\gamma\gamma$ angular correlation measurements discussed in Sec. II. Angular-distribution functions $W(\Theta_1, \Theta_2, \Phi)$ of two coincident γ-ray transitions are fitted to experimental γ-ray intensity distributions obtained by gates on depopulating transitions in the $\gamma\gamma$-coincidence matrices of eight angular-correlation groups. Figure 5(d) shows a benchmark angular-correlation fit of the 727-keV decay, gated on the 773-keV $E2$ transition in ^{132}Xe. The fit of a $5^+ \xrightarrow{\delta} 4^+ \xrightarrow{E2} 2^+$ hypothesis yields a good agreement with the experimental distribution. Moreover, the obtained $E2/M1$ multipole-mixing ratio of

$\delta_{\text{exp.}} = 0.44(7)$ agrees well with the evaluated value of $\delta = 0.41^{+7}_{-8}$ [56].

Similarly, keeping the spin of the 3357- and the 3707-keV state in ^{136}Ba fixed, spins of $J = 11$, 12, and 13 were tested for the $E_x = 4217$-keV state. One multipole-mixing ratio δ in the $J_1 \xrightarrow{\delta_1} J_2 \xrightarrow{\delta_2} J_3$ cascade is fixed while the other is varied in order to avoid an overdeterminacy of the fit. For a parity-changing $E1$ transition, a multipole-mixing ratio in the order of $\delta \approx 0$ is expected. Scenarios of $11 \xrightarrow{\delta_1=0} 11 \xrightarrow{\delta_2} 10$ and $12 \xrightarrow{\delta_1=0} 11 \xrightarrow{\delta_2} 10$ for the 510-349-keV cascade yield χ^2 values of 10 and 14. Obviously, a parity-changing 510-keV $E1$ transition can be rejected. Moreover, a $13 \xrightarrow{\delta_1=0} 11 \xrightarrow{\delta_2} 10$ assumption does not fit the experimental data, which excludes an $E2$ transition with 510 keV. Vice versa, keeping $\delta_2 = 0$ fixed, a much better agreement is obtained. Figure 5(e) visualizes the angular-correlation distribution for the 510-349 keV cascade in ^{136}Ba with respect to the different groups. The $12 \xrightarrow{\delta_1} 11 \xrightarrow{\delta_2=0} 10$ hypothesis with $\delta_1 = -0.15(6)$ ($\chi^2 = 1.1$) gives the best agreement with the experimental $W(\Theta_1, \Theta_2, \Phi)$ distribution in all correlation groups. Thus, a spin of $J = 12$ is assigned to the 4217-keV state. Apart from that, similar fits assuming a larger fixed δ_2 value for the 349-keV transition yield significantly worse χ^2 values of the $12 \xrightarrow{\delta_1} 11 \xrightarrow{\delta_2} 10$ hypothesis (i.e., $\delta_2 \equiv \pm 0.05$; $\chi^2 > 2.6$ and $\delta_2 \equiv \pm 0.1$; $\chi^2 > 3.3$). Hence, on the basis of a pure-dipole character for the 349-keV γ-ray as shown in Fig. 5(c) and the overall agreement with the shell-model calculations presented in Sec. IV A, a parity changing $E1$ transition is proposed leading to a negative parity assignment of the 3707-keV state.

Employing the same method, the spin of the newly established excited state at $E_x = 4921$ keV is determined, as shown in Fig. 5(f). Spins of $J = 11$, 12, and 13 are tested. Assuming $\delta_2 = 0$, the 1214-349-keV cascade is best reproduced by a $12 \xrightarrow{\delta_1} 11 \xrightarrow{\delta_2} 10$ sequence with $\delta_1 = -0.01(12)$. Vice versa, keeping $\delta_1 = 0$ fixed, δ_2 is determined to be in agreement with zero. The obtained χ^2 values of both fits are similar, showing the mutual consistency of both hypotheses. Consequently, similar to the negative-parity $E_x = 4217$-keV state, the $E_x = 4920$-keV state has a spin of $J = 12$. The pure dipole character of the 1214-keV transition suggests a $E1$ character of this transition, indicating that the $E_x = 4920$-keV state has different spin than the $E_x = 3707$-keV state and is therefore most probably of positive parity. Moreover, the independently measured 1214-349-keV cascade supports a pure-dipole $E1$ 349-keV transition.

The $\gamma\gamma$ angular-correlation analysis is further exploited to verify the validity of the 297-1380-keV cascade on top of the $J^\pi = 7^-$ isomer. The spin of the initial $J = 11$ state and that of the final $J = 7$ state are fixed. A spin assumption of $J = 9$ for the $E_x = 3410$-keV state yields a χ^2 value of 1.8, compared to χ^2 values of 2.2 and 2.3 for $J = 10$ and $J = 8$ hypotheses. Since an $E3$ or $M2$ transition in this cascade would corroborate another isomer, a spin assignment of $J = 9$ for the $E_x = 3410$-keV state is necessary to keep a prompt decay character. Consequently, the angular-correlation measurement supports the 297-1380-keV cascade in ^{136}Ba.

B. ^{137}Ba

In a previous work by this group [20], the level scheme of ^{137}Ba above the $J^\pi = 19/2^-$ isomer was extended to the structure presented in Fig. 2(b), using the $\gamma\gamma$ coincidences from the ^{11}B + ^{130}Te experiment introduced in Sec. II D. This paper focuses on the angular-distribution and angular-correlation analysis of this data set. Note that the new determined spins and parity of the high-spin states is based on the tentative $J^\pi = 19/2^-$ assignment of the isomeric 2350-keV state in ^{137}Ba given in Refs. [20,21]. However, the assignment is strongly supported by systematics and shell-model calculations.

Due to the low cross section of the $p3n$ evaporation channel, the basis of the data analysis are double-γ HPGe coincidences to reduce the complexity of the γ-γ spectra of the different rings of the HORUS setup. The fusion-evaporation reaction orients the spin of the initial level with respect to the beam axis. However, according to the very long half-life of the $J^\pi = 19/2^-$ state, the 120-1568-keV cascade is no longer aligned with respect to the beam axis; it decays instead isotropic. Thus, a γ-ray gate on 1568 keV does affect the alignment with respect to the beam axis for coincident transitions above the isomer.

To verify that the spins above the isomer are still aligned with respect to the beam axis, a benchmark angular γ-ray distribution of the well-known 1172-keV ($23/2^- \xrightarrow{E2} 19/2^-$ [54]) transition in ^{137}La is shown in Fig. 6(a). The intensities in the different rings are extracted from the corresponding γ-ray spectra, gated on the 782-keV ($15/2^- \rightarrow 11/2^-$) transition, located below the $J^\pi = 19/2^-$ [$T_{1/2} = 360(40)$ ns [57]] isomer. A good agreement between measured and theoretical intensity distribution of a pure quadropole transition is demonstrated.

In ^{137}Ba the $J^\pi = 19/2^-$ [$T_{1/2} = 0.589(20)$ μs [20]] isomer decays via a 120-1568-keV cascade. Applying a 1568-keV gate to all rings, comparisons between measured and theoretical angular distributions for the 275- and 1195-keV transitions in ^{137}Ba are shown in Figs. 6(b) and 6(c). In both cases, the highest intensity was measured in the detectors perpendicular to the beam axis, which is opposite to the distribution of the benchmark quadrupole transition presented in Fig. 6(a). Therefore, both experimentally determined intensity distributions are incompatible with a quadrupole $23/2 \xrightarrow{\Delta I=2} 19/2$ transition. Also an $E3$ transition can be clearly rejected for both γ rays, since the Weisskopf half-life estimate is several orders of magnitude larger compared to a competitive quadrupole transition. Moreover, pure as well as mixed quadrupole/dipole $19/2 \xrightarrow{\Delta I=1,2} 19/2$ transitions do not fit the experimental data. Overall, a $J = 21/2$ hypothesis for both initial states match the experimental values best.

Spins of the 2913- and 3841-keV states are determined using the $\gamma\gamma$-coincidence angular-correlation technique. The number of groups has to be reduced in order to perform

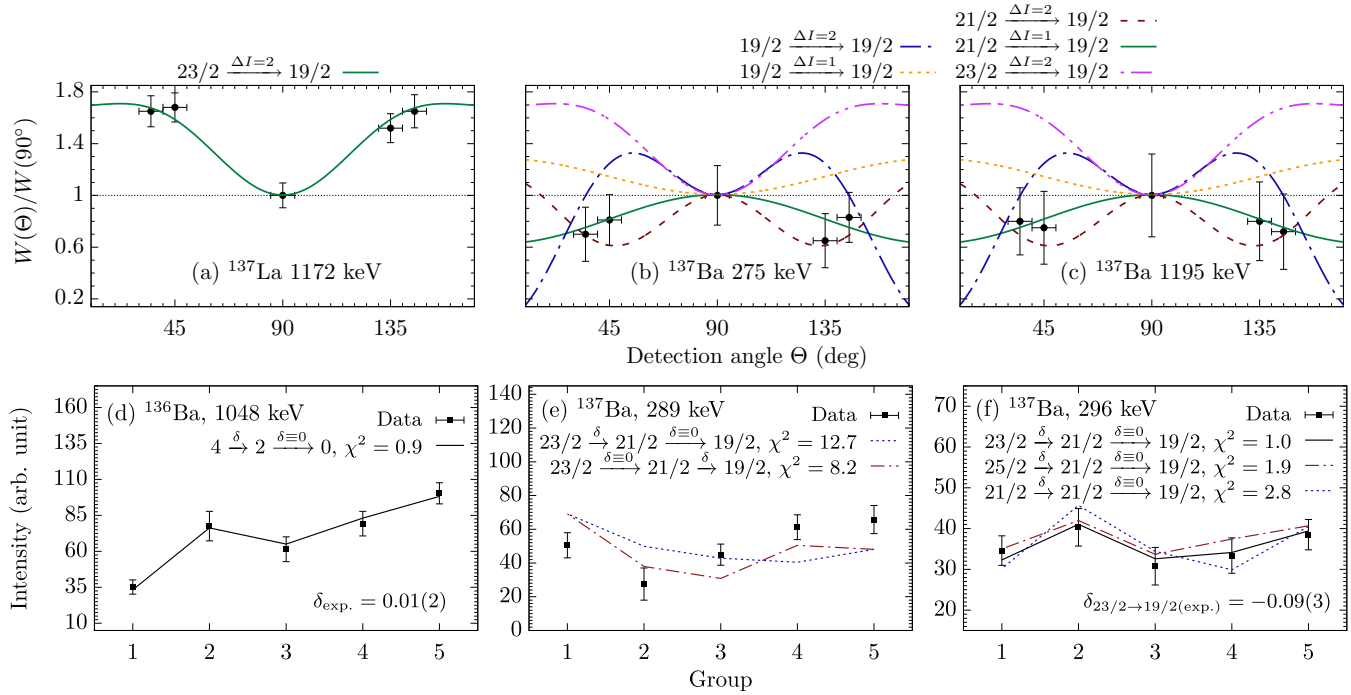

FIG. 6. Angular distributions of transitions in ^{137}La and ^{137}Ba. Experimental distribution is obtained in the γ-ray spectra, gated on disoriented transitions below the isomers. (a) Benchmark angular distribution of the well-known 1172-keV ($23/2^- \rightarrow 19/2^-$) γ-ray transition in ^{137}La. The pure quadrupole hypothesis is well reproduced with this approach. Angular distribution of (b) 275- and (c) 1195-keV transition, decaying into the $19/2^-$ isomer in ^{137}Ba. Intensities are extracted from $\gamma\gamma$ coincident spectra with a gate on the $15/2^- \rightarrow 11/2^-$ transition. Several pure dipole and quadrupole hypotheses (lines) are plotted. (d) Benchmark $\gamma\gamma$ angular correlations for the $4_1^+ \rightarrow 2_1^+ \rightarrow 0_1^+$ (1048-818-keV) cascade in ^{136}Ba. Investigation for (e) the 289-275-keV cascade and (f) the 296-1195-keV cascade in ^{137}Ba. Several spin hypotheses are plotted.

angular-correlation measurements in the elusive Ba channels. To ensure the quality of the angular-correlation analysis, a benchmark fit of the well-established $4^+ \rightarrow 2^+ \rightarrow 0^+$ cascade in ^{136}Ba is presented in Fig. 6(d). The $E2$ character of the 1048-keV transition is well reproduced.

The singles γ-ray angular-distribution measurement suggested a spin of $J = 21/2$ for both the 2624- and 3545-keV state [cf. Fig. 6(b) and 6(c)]. Consequently, the spin values of the 2913- and 3841-keV states are limited to $J = 21/2$, $23/2$, and $25/2$. Figure 6(e) shows the experimental angular-correlation distribution of the 289-keV transition in the different groups, gated on the 275-keV transition. Assuming a vanishing multipole-mixing ration ($\delta_1 = 0$) of the 289-keV transition and a variable δ_2 value of the 275-keV transition, fits of the three aforementioned hypotheses results in χ^2 values larger than 4. Furthermore, fixing the 275-keV transition to a dipole character ($\delta_2 = 0$) and varying the δ_1 value of the 289-keV transition, χ^2 values larger than 6 were obtained. Since the 275- and 289-keV transitions are incompatible with a multipole-mixing ratio of zero, a parity-changing $E1$ character of the 275- or 289-keV transition can be ruled out. Likewise, a parity-conserving $E2$ character with a spin change from $J = 25/2$ to $J = 21/2$ for the 289-keV transition is not compatible with the experimental distribution. Figure 6(e) shows two examples for fits with corresponding χ^2 values of 12.7 and 8.2. Since the 289-275-keV cascade built on the $J^\pi = 19/2^-$ state has no parity-changing character, we propose negative-parity states $J^\pi = 21/2^-$ at $E_x = 2624$-keV and $J^\pi = 23/2^-$ at $E_x = 2913$-keV.

Figure 6(f) shows the experimentally deduced angular-correlation intensity distribution for the coincident γ rays at 1195 and 296 keV, compared to calculated values for different scenarios of the spin and parity of the 3841-keV state. Fixing the spin value of the 3545-keV state to $J = 21/2$, hypotheses with pure dipole character ($21/2 \xrightarrow{\delta_1=0} 21/2$ or $23/2 \xrightarrow{\delta_1=0} 21/2$) as well as a pure quadrupole character ($25/2 \xrightarrow{\delta_1=0} 21/2$) yield a limited agreement with the data. Instead, a good match is obtained by assuming a dominant dipole component ($\delta_2 = 0$) for the $21/2 \rightarrow 19/2$ 1195-keV transition and a nonzero δ_1 value for the 296-keV transition. A hypothesis of $J = 23/2$ for the $E_x = 3841$ keV state yields the best result. The nonvanishing multipole-mixing ratio $\delta_1 = -0.09(3)$ clearly indicates that the 296-keV transition is parity conserving. Assuming a nonzero fixed δ_2 value of the 1195-keV transition and a variable δ_1 value of the 296-keV transition, the χ^2 value of the $23/2 \xrightarrow{\delta_1} 21/2 \xrightarrow{\delta_2} 19/2$ hypothesis get larger (i.e., $\delta_2 = \pm 0.05$; $\chi^2 > 2.2$ and $\delta_2 = \pm 0.1$; $\chi^2 > 2.9$). Based on the results of the shell-model calculations presented in Sec. IV B, this observation supports a pure-dipole $E1$ 1195-keV transition which is in line with a change from negative to positive parity.

IV. SHELL MODEL

The extended level schemes of ^{136}Ba and ^{137}Ba are compared with the results of shell-model theory. All shell-model calculations were carried out in an untruncated $gdsh$ valence space outside doubly magic ^{100}Sn, employing the shell-model code NUSHELLX@MSU [58], the massive-parallelization code KSHELL [59], and the ANTOINE shell-model code [60].

The first calculation is conducted with the effective interaction GCN50:82 [61,62]. The interaction is derived from a realistic G matrix based on the Bonn-C potential [63]. Empirical monopole corrections to the original G matrix are introduced by fitting different combinations of two-body matrix elements to sets of experimental excitation energies from even-even and even-odd semimagic nuclei.

The second calculation is conducted in the framework of the realistic shell model [64,65], denoted as realistic SM. Single-particle energies and two-body effective interaction are determined from the established CD-Bonn free nucleon-nucleon potential [63] using the $V_{\text{low-}k}$ approach with a cutoff momentum of $\Lambda = 2.6$ fm^{-1}, plus the Coulomb force for protons. The effective shell-model Hamiltonian is derived iteratively by means of the many-body perturbation theory in the $\hat{Q}$-box folded diagram expansion, including all diagrams up to third order in the interaction. More details can be found in Ref. [66].

A third calculation is performed utilizing the framework of the pair-truncated shell model, denoted as PQM130 (Pairing+QQ+Multipole for mass region 130). The approach leverages a pairing-plus-quadrupole interaction that consists of spherical single-particle energies, a monopole pairing, a quadrupole pairing, and a quadrupole-quadrupole interaction. The Hamiltonian in each neutron and proton space is diagonalized separately and afterwards the total Hamiltonian is diagonalized in the truncated space. More details on the calculation are given in Refs. [67,68].

Another calculation is carried out with the jj55pn Hamiltonian (referred to as the SN100PN interaction) [69]. The Hamiltonian consists of four terms covering the neutron-neutron, neutron-proton, proton-proton, and Coulomb repulsion between the protons individually. A renormalized G matrix derived from the CD-Bonn interaction [63] was employed to construct the realistic two-body residual interaction. The proton and neutron single-particle energies are based upon the energy levels in ^{133}Sb and ^{131}Sn.

A. ^{136}Ba

As a first benchmark for the validity of the shell-model results in the high-spin regime, reduced transition probabilities $B(E2; 10^+_1 \rightarrow 8^+_1)$ are calculated with the GCN50:82, Realistic SM, and SN100PN interactions. Effective charges are chosen as $e_\pi = 1.82$ and $e_\nu = 0.82$ in the GCN50:82 and SN100PN interaction, while an effective microscopic $E2$ operator, derived consistently with the effective Hamiltonian, is employed in realistic SM. The effective charge values are equal to the charges used in a previous study of ^{136}Ba [3].

The calculated $B(E2; 10^+_1 \rightarrow 8^+_1)$ values of 0.81 e^2 fm^4 (GCN50:82), 0.44 e^2 fm^4 (SN100PN), and 0.22 e^2 fm^4 (realistic SM) are in reasonable agreement with the previously reported experimental values of 0.97(2) e^2 fm^4 [3] and 0.96(10) e^2 fm^4 [14]. The agreement between the calculated and experimental $B(E2; 10^+_1 \rightarrow 8^+_1)$ values has improved considerably compared to the shell-model calculations conducted in Ref. [3].

Calculated level energies of four shell-model calculations are compared to the experimental levels of ^{136}Ba, as shown in Fig. 7 [(c) GCN50:82; (d) PQM130; (e) realistic SM; and (f) SN100PN]. Since states above the $J^\pi = 10^+$ isomer are the subject of this discussion, only these states are displayed. However, also the excitation energies of the yrast states $J^\pi = 2^+$, 4^+, 6^+, and 8^+ at excitation energies of $E_x = 819$, 1867, 2207, and 2994 keV are well reproduced. The different shell-model calculations locate the corresponding states at energies of $E_x = 842$, 1873, 2195, 3036 (GCN50:80), $E_x = 1041$, 1959, 2297, 3209 (realistic SM), $E_x = 814$, 1638, 2230, 3109 (PQM130), and $E_x = 893$, 1896, 2083, 2959 keV (SN100PN).

The calculations predict the $J^\pi = 10^+_1$ state with the $\nu h^{-2}_{11/2}$ configuration at excitation energies of 3332 (GCN), 3354 (realistic SM), 3164 (PQM130), and 3126 keV (SN100PN), which are in good agreement with the experimentally determined energy of 3357 keV. In particular, the GCN50:82 interaction provides an excellent agreement with the well-known yrast states $J^\pi \leqq 10^+$. Larger discrepancies between the calculations emerge in the high-spin regime; e.g., the predictions for the first excited $J^\pi = 12^+$ state differs by 0.5 MeV.

The angular-correlation and angular-distribution measurements in Sec. III A indicated a $J^\pi = 11$ assignment for the 3707-keV state and a pure-dipole character for the 349-keV transition. It is noteworthy that all interactions do not predict a yrast positive-parity state with spin $J > 10$ until approximately 1 MeV above the $J^\pi = 10^+$ state. However, all four interactions yield excited $J^\pi = 10^+_2$, 10^-_1, and 11^-_1 states only a few hundred keV above the isomer. Moreover, $J^\pi = 11^+$ states are coherently predicted at higher energies than the $J^\pi = 11^-$ states. Accordingly, a parity-changing $E1$ transition is proposed and the state at $E_x = 3707$ keV is identified as the $J^\pi = 11^-$ state, based on these theoretical findings. Assuming a proceeding negative-parity character of this band, the states at $E_x = 4782$ and $E_x = 4878$ keV, decaying parallel into the $J^\pi = 12^-$ 4217-keV state, can most likely be interpreted as the first and second excited $J^\pi = 13^-$ states.

In the calculations the energy difference between the $J^\pi = 12^+_1$ and $J^\pi = 10^+_1$ state amount to 1555 (GCN50:82), 1551 (realistic SM), 1543 (PQM130), and 1442 keV (SN100PN). The calculated values are in good agreement with the experimentally observed energy difference of 1562 keV between the $J^\pi = 10^+_1$ and the $E_x = 4920$-keV state. In the aforementioned discussion of Fig. 5(f) a pure-dipole character of the 1214-keV transition was confirmed, which suggests a parity change. Combining this experimental result with the shell-model results, the $E_x = 4920$-keV state is clearly assigned to $J^\pi = 12^+$.

On top of the $E_x = 4921$-keV state, a low-energy 328-130-144-keV cascade is observed. The calculated transition

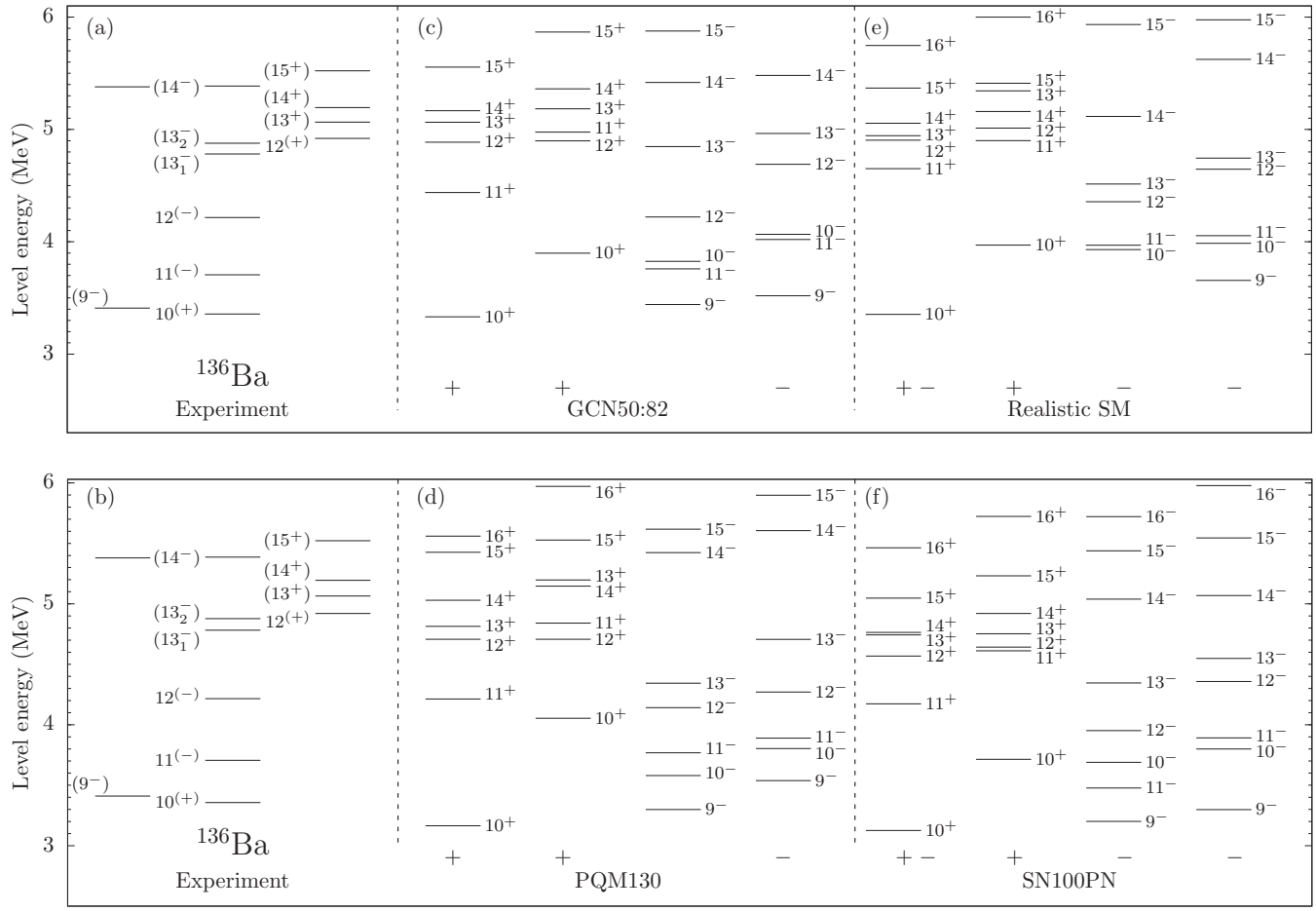

FIG. 7. Comparison of experimental energy spectra with the results of shell-model calculations for ^{136}Ba. Only states above the $J^\pi = 10^+$ state are displayed. For clarity, the states are separated into columns for positive- and negative-parity states, as well as for yrast and yrare states. (a),(b) Experimental energy spectra, shell-model results obtained with (c) GCN50:82, (d) PQM130, (e) realistic SM and, (f) SN100PN interactions.

energies in the $15^+ \to 14^+ \to 13^+ \to 12^+$ cascade are 388-103-177 (GCN), 314-111-39 (realistic SM), 397-215-106 (PQM130), and 233-111-135 keV (SN100PN), respectively. According to the good agreement between calculated and experimental energy differences, the 328-130-144-keV cascade can most likely be attributed to the $15^+ \to 14^+ \to 13^+ \to 12^+$ sequence. Shell-model calculations suggest a dominant $M1$ character for this band; i.e., GCN50:82 predicts multipole-mixing ratios of $\delta_{15\to14} = -0.05$, $\delta_{14\to13} = -0.01$, and $\delta_{13\to12} = -0.02$ which are very similar to the values calculated with SN100PN. In the calculations $J^\pi = 9^-$ states are predicted slightly above the $J^\pi = 10^+$ isomer. In accordance with the angular-correlation measurement, a tentative spin assignment of $J^\pi = (9^-)$ for the $E_x = 3410$-keV state is made.

The shell-model results provide insight into the structure of the levels built on top of the isomeric $J^\pi = 10^+_1$ state. The nuclear structure of ^{136}Ba and the $-2p$ isotone ^{134}Xe have similar characteristics. Figure 8 shows a detailed decomposition of several states into their proton and neutron configurations in (a)–(f) ^{136}Ba and (g)–(l) ^{134}Xe computed with GCN50:82 (filled blue boxes) and SN100PN (empty red boxes). The decomposition of the total angular momentum of states in ^{134}Xe and ^{136}Ba are presented in Figs. 9(a)–9(l) indicating which nucleon pairs are broken to obtain the total angular momentum of the calculated states.

Although more fragmented in ^{136}Ba, the configurations resemble the ones in ^{134}Xe. In the different positive- and negative-parity states, protons are easily redistributed from $g_{7/2}$ to $d_{5/2}$, i.e., these orbitals are energetically close together.

The configurations of the $J^\pi = 8^+_1$ state in ^{134}Xe and ^{136}Ba are predicted to be highly fragmented in both calculations, as displayed in Figs. 8(a) and 8(g). In ^{134}Xe, the four valence protons mainly occupy the $\pi(g^4_{7/2})$ and the $\pi(g^3_{7/2}d^1_{5/2})$ configuration. The total angular momentum of the $J^\pi = 8^+$ state is mainly generated from these configurations in the proton space, as visible in Fig. 9(g). Excitations into the proton $h_{11/2}$ orbital can be neglected (<2%). Using GCN50:82, the neutron configurations $\nu h^{-2}_{11/2}$, $\nu(h^{-1}_{11/2}s^{-1}_{1/2})$, and $\nu d^{-2}_{3/2}$ account for 20%, 10%, and 16% of the overall configuration in the $J^\pi = 8^+_1$ state in ^{136}Ba, respectively. In the realistic-SM calculation main configurations are couplings of the $\pi(g^5_{7/2}d^1_{5/2})$ proton configuration to (17%) $\nu d^{-2}_{3/2}$ and (15%) $\nu h^{-2}_{11/2}$, which is in good agreement with the results of the GCN50:82 and

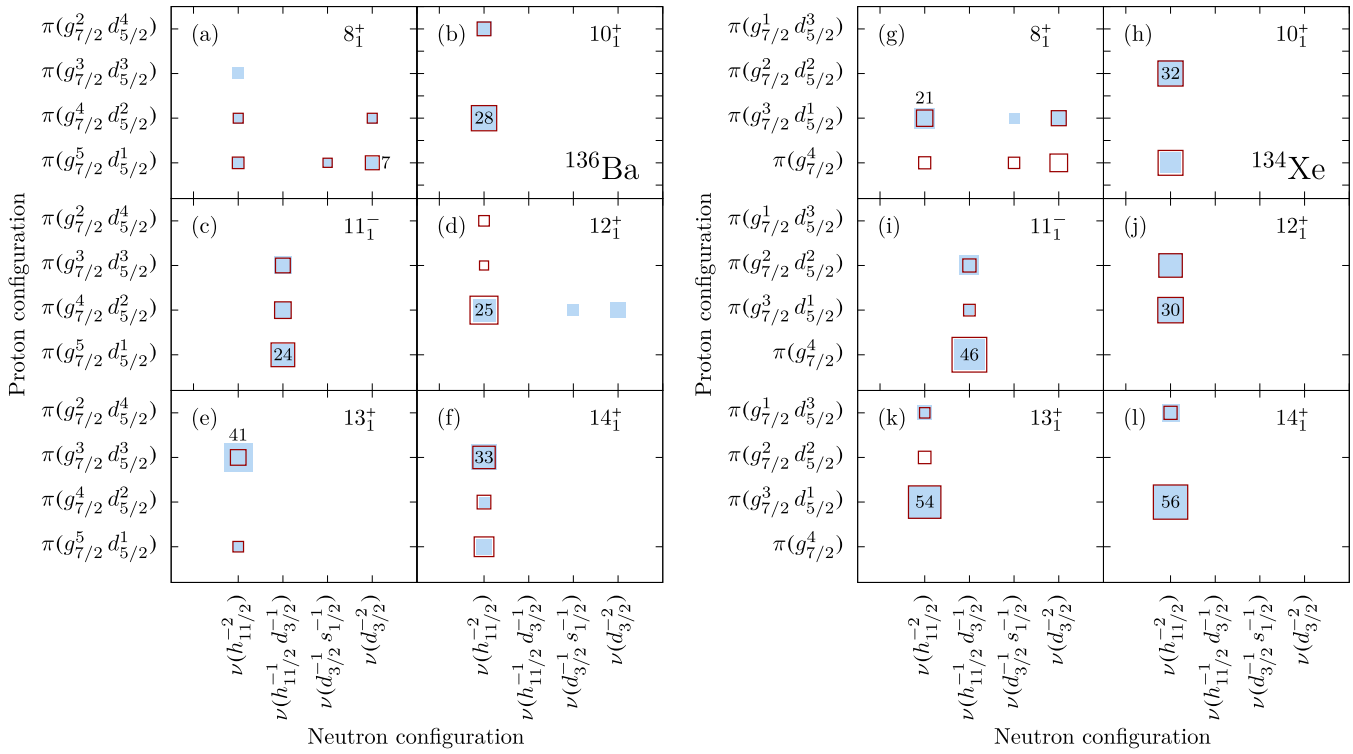

FIG. 8. Decomposition of the total wave function configuration into its proton and neutron components for several positive- and negative-parity states in (a)–(f) ^{136}Ba and (g)–(l) ^{134}Xe, employing the GCN50:82 (filled blue boxes) and the SN100PN interaction (empty red boxes). Strongest components in the GCN50:82 interaction are labeled with corresponding percentages. The other configurations of both calculations are drawn with areas proportional to their percentages.

SN100PN calculations. Similarly to ^{134}Xe, the $J^\pi = 8^+$ state in ^{136}Ba is dominated by proton spins of (45%) $I_\pi = 8$ and (37%) $I_\pi = 6$, as displayed in Fig. 9(a).

The wave function of the isomeric $J^\pi = 10^+_1$ state in ^{136}Ba is dominated by the neutron $\nu(h^{-2}_{11/2})$ configuration with spins of 56% $\nu_{10^+} \otimes \pi_{0^+}$ and 30% $\nu_{10^+} \otimes \pi_{2^+}$. A major $\nu(h^{-2}_{11/2})$ configuration for the $J^\pi = 10^+_1$ state is also in accordance with the SN100PN and realistic SM calculations. Significant deviations between the calculations arise for the $J^\pi = 12^+_1$ state in ^{136}Ba. The decomposition matrix of the $J^\pi = 12^+_1$ bandhead of the positive-parity band computed by the GCN50:82 interaction, displayed in Fig. 8(d), shows an additional occupation of the neutron $d_{3/2}$ and $s_{1/2}$ orbital, which reduces the occupation of the $\nu(h^{-2}_{11/2})$ configuration.

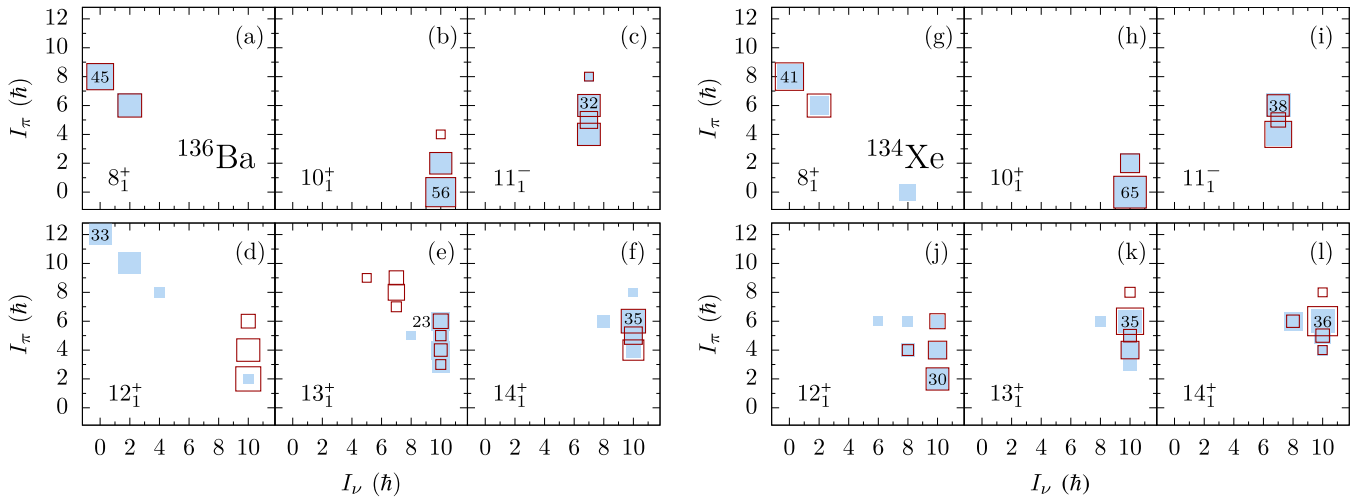

FIG. 9. Decomposition of the total angular momentum of selected states of (a)–(f) ^{136}Ba and (g)–(l) ^{134}Xe, using the GCN50:82 interaction (filled blue boxes) and the SN100PN interaction (empty red boxes) into their proton and neutron spins.

A declining impact of the $\nu(h_{11/2}^{-2})$ configuration of the $J^\pi = 12_1^+$ state in ^{136}Ba is also predicted by the realistic SM where $\pi(g_{7/2}^5 h_{11/2}^1) \otimes \nu(d_{3/2}^{-1} h_{11/2}^{-1})$ is computed as the main configuration with a probability of 51%. However, the SN100PN interaction does not predict a change of neutron occupation between the $J^\pi = 10_1^+$ and $J^\pi = 12_1^+$ states. Such discrepancies between both calculations are not observed for states in ^{134}Xe.

The differences in the predicted structure of the $J^\pi = 12^+$ state is mirrored in the spin composition, as visible in Fig. 9(d). While the SN100PN interaction predicts a dominant neutron spin of (91%) $I_\nu = 10^+$, the GCN50:82 predicts this fully aligned neutron-spin configuration to be insignificant (7%). Instead, major contributions stem from $\pi_{12^+} \otimes \nu_{0^+}$ and $\pi_{10^+} \otimes \nu_{2^+}$. The proton spin is generated dominantly by the $\pi(g_{7/2}^4 d_{5/2}^2)$ configuration with a maximum spin contribution of $I_\pi = 12$. The proton $h_{11/2}$ orbital does not contribute considerably (<2%) to the configuration of the $J^\pi = 12^+$ state using GCN50:82.

Going to higher spins along the positive-parity band, a strong $\nu(h_{11/2}^{-2})$ contribution returns to prevail for $J^\pi \geqslant 13_1^+$ states in the GCN50:82 calculation. Configurations including the neutron $d_{3/2}$ orbital become negligibly small in the GCN50:82 and SN100PN interactions. In contrast, the leading neutron configuration of the negative-parity states with $J^\pi > 10_1^-$ is $\nu(h_{11/2}^{-1} d_{3/2}^{-1})$. The neutron $\nu(h_{11/2}^{-2})$ configuration nearly vanishes in the decomposition of the negative-parity states.

The role of the different proton and neutron orbitals is further scrutinized by investigating the evolution of average occupation numbers of neutrons in the *gdsh* model space for several high-spin states in $N = 80$ isotones, as listed in Table II. In all even-mass isotones from ^{134}Xe to ^{138}Ce, the average occupation of the neutron $h_{11/2}$ orbital for the $J^\pi = 10^+$ states is $N_\nu \approx 10$, indicating a two-neutron $\nu h_{11/2}^{-2}$ configuration. However, in the GCN50:82 and realistic SM interactions, the $\nu d_{3/2}$ orbital is gaining significance for the $J^\pi = 11_1^-$ and 12_1^+ states from ^{136}Ba onwards. Furthermore, both states have only one neutron hole in the $\nu h_{11/2}$ orbital ($N_\nu \approx 11$). For completeness, the corresponding average occupation of the neutron $d_{3/2}$, $s_{1/2}$, and $h_{11/2}$ orbitals in the realistic SM calculation have values of 3.12, 1.99, 11.01 for the $J^\pi = 11_1^-$ state and 3.23, 1.87, 11.00 for the $J^\pi = 12_1^+$ state, respectively. Accordingly, proton configurations are vital to generate the spin, which is consistent with the results presented in Figs. 8(c) and 8(d). Hence, the configuration of the $J^\pi = 12_1^+$ state in ^{136}Ba, calculated by GCN50:82 and realistic SM, mirrors the configuration of the $J^\pi = 11_1^-$ state rather than that of the $J^\pi = 10_1^+$ state, which supports a decay of the $J^\pi = 12_1^+$ state into the $J^\pi = 11_1^-$ state.

The dominating proton configuration of the yrast $J^\pi = 8^+$ state causes the isomeric character of the two-neutron hole $J^\pi = 10_1^+$ state [3]. In a similar way, the unobserved $12^+ \rightarrow 10^+$ transition can be understood microscopically. ^{136}Ba is the lowest-mass isotone along the $N = 80$ chain in which an angular momentum of $J = 12$ can be generated exclusively from protons in the $g_{7/2}$ and $d_{5/2}$ orbitals [i.e., $\pi(g_{7/2}^4 d_{5/2}^2)$]. The dominating proton configuration of the $J^\pi = 12^+$ state, as calculated by the GCN50:82 interaction and the realistic-SM interaction, hinders a decay into the two-neutron hole $J^\pi = 10^+$ state. Calculated reduced transition probabilities $B(E2; 12^+ \rightarrow 10^+)$ underpin the reliability of the GCN50:82 and realistic-SM interaction. Corresponding values are compatible in ^{134}Xe (215 e^2 fm^4 with GCN50:82 and 222 e^2 fm^4 with SN100PN), while they differ significantly in ^{136}Ba: The larger proton component in the $J^\pi = 12^+$ state causes a lower $B(E2; 12^+ \rightarrow 10^+)$ value of 62 e^2 fm^4 in the GCN50:82 and of 3 e^2 fm^4 in the realistic-SM calculation, compared to $B(E2; 12^+ \rightarrow 10^+) = 375\, e^2$ fm^4 using SN100PN. The low $B(E2; 12^+ \rightarrow 10^+)$ values in the GCN50:82 and realistic-SM calculations is in agreement with the experimentally unobservability of this transition.

Interestingly, adding two protons to ^{136}Ba, the occupation number of $N_\nu \approx 11$ for the neutron $h_{11/2}$ orbital in Table II indicates that the SN100PN interaction predicts an emerging proton component for the $J^\pi = 12^+$ state in ^{138}Ce.

TABLE II. Average neutron occupation numbers in each single-particle orbit of the *gdsh* model space for observed high-spin states in ^{134}Xe, ^{136}Ba, and ^{138}Ce using the GCN50:82 and SN100PN interaction.

Isotope	J^π	$g_{7/2}$	$d_{5/2}$	$d_{3/2}$	$s_{1/2}$	$h_{11/2}$
			GCN50:81			
^{134}Xe	10_1^+	8.00	6.00	4.00	2.00	10.00
	11_1^-	7.97	5.97	3.06	1.99	11.00
	12_1^+	8.00	6.00	4.00	2.00	10.00
^{136}Ba	10_1^+	7.99	5.99	4.00	2.00	10.03
	11_1^-	7.96	5.96	3.09	1.99	11.00
	12_1^+	7.87	5.86	3.57	1.79	10.91
^{138}Ce	10_1^+	7.98	5.98	3.99	2.00	10.05
	11_1^-	7.94	5.95	3.11	1.99	11.00
	12_1^+	7.94	5.96	3.16	1.94	11.00
			SN100PN			
^{134}Xe	10_1^+	8.00	6.00	4.00	2.00	10.00
	11_1^-	7.98	5.96	3.07	1.99	11.00
	12_1^+	8.00	6.00	4.00	2.00	10.00
^{136}Ba	10_1^+	8.00	6.00	4.00	2.00	10.00
	11_1^-	7.97	5.95	3.11	1.98	11.00
	12_1^+	8.00	5.99	3.99	2.00	10.03
^{138}Ce	10_1^+	7.99	5.99	4.00	2.00	10.02
	11_1^-	7.95	5.93	3.13	1.99	11.00
	12_1^+	7.96	5.94	3.21	1.89	11.00

B. ^{137}Ba

Calculated level energies for states above the $J = 19/2^-$ isomer in ^{137}Ba [(c) GCN50:82; (d) PQM130; (e) realistic SM and (f) SN100PN], are compared to experimental level energies in Fig. 10. The pivotal $J = 11/2^-$ neutron-hole isomer at $E_x = 662$ keV is predicted at excitation energies of 534 (GCN50:82), 643 (realistic SM), 692 (PQM130), and 478 keV (SN100PN). The shell-model calculations compute the 120-1567-keV cascade to have γ-ray energies of 285-1396 (GCN50:82), 412-1491 (PQM130), and 231-1396 keV

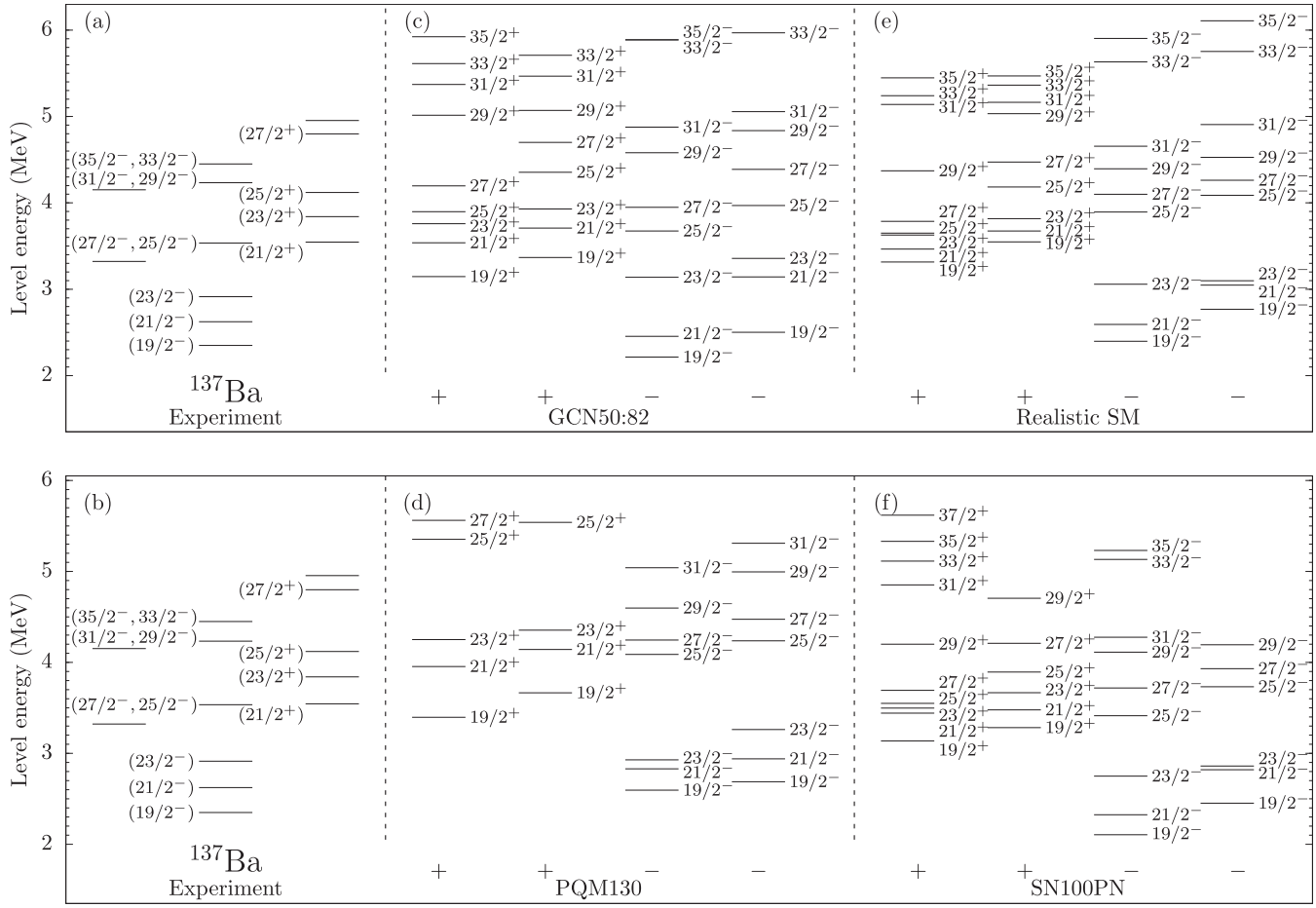

FIG. 10. Comparison of experimental energy spectra with the results of shell-model calculations for ^{137}Ba. Only states above the $J^\pi = 19/2^-$ state are displayed. For clarity, the states are separated into columns for positive- and negative-parity states, as well as for yrast and yrare excited states. (a),(b) Experimental energy spectra, shell-model results obtained with (c) GCN50:82, (d) PQM130, (e) realistic SM, and (f) SN100PN interactions.

(SN100PN). Going to higher spins, the energy differences in the four calculations between states of same spin and parity amount for up to 1 MeV.

In the calculated excitation pattern, the $J^\pi = 21/2^-_1$ states emerge at 240 (GCN50:82), 195 (realistic SM), 234 (PQM130), and 220 keV (SN100PN) above the $J^\pi = 19/2^-_1$ states. Moreover, $J^\pi = 23/2^-_1$ states are predicted 684 (GCN50:82), 465 (realistic SM), 100 (PQM130), and 425 keV (SN100PN) higher in excitation energy with respect to the $J^\pi = 21/2^-_1$ state. In accordance with the results of $\gamma\gamma$ angular-correlation measurements [see Figs. 6(b) and 6(e)], which confirmed mixed $M1/E2$ 289- and 275-keV transitions and therefore a parity-conserving 289-275-keV cascade, the $E_x = 2624$- and $E_x = 2913$-keV states are identified as the first excited $J^\pi = 21/2^-$ and $23/2^-$ states, respectively.

Going to higher spins along the negative-parity band, in particular GCN50:82 tend to group pairs of yrast spins ($J^\pi = 25/2^-$, $27/2^-$) and ($J^\pi = 29/2^-$, $31/2^-$). Both groups are separated by a larger energy gap compared to the energy gaps between both states within the group. This observation associates the $E_x = 3611$-keV state with $J^\pi = (25/2^-, 27/2^-)$ and the $E_x = 4233$-keV state with $J^\pi = (29/2^-, 31/2^-)$.

Similar to the $E_x = 2624$-keV state, also the spin of the $E_x = 3545$-keV state is measured to be of spin $J = 21/2$ [see Fig. 6(c)]. Positive-parity states of similar spin ($J \geqslant 19/2^+_1$) are calculated to appear at higher excitation energy than the $J^\pi = 19/2^-_1$ state. The energy difference between the $J^\pi = 19/2^-_1$ and $21/2^+_1$ states is predicted to be 1323 (GCN50:82), 1067 (realistic SM), 1360 (PQM130), and 1337 keV (SN100PN). In accordance with the experimental results obtained in the angular-correlation and angular-distribution investigations [see Figs. 6(c) and 6(f)], the state at $E_x = 3545$ keV is interpreted as the first excited $J^\pi = 21/2^+$ state and, thus, as the bandhead of the positive-parity band.

Moreover, assuming a $J = 23/2$ assignment for the 3841-keV state, the multipole-mixing ratio of the 296-keV transition is measured as $\delta = -0.09(3)$ which suggests that the 3841-keV state has the same parity as the 3545-keV state [see Fig. 6(f)]. Excited $J = 23/2^+_1$ states are calculated 152 to 453 keV above the $J = 21/2^+_1$ states. Consequently, a spin of $J^\pi = 23/2^+$ for the $E_x = 3841$-keV state is in agreement with shell-model calculations.

Due to the large density of predicted states above 4 MeV, no unambiguous assignment for the $E_x = 4120$- and 4799-keV states is possible. Since both states do not exhibit decay

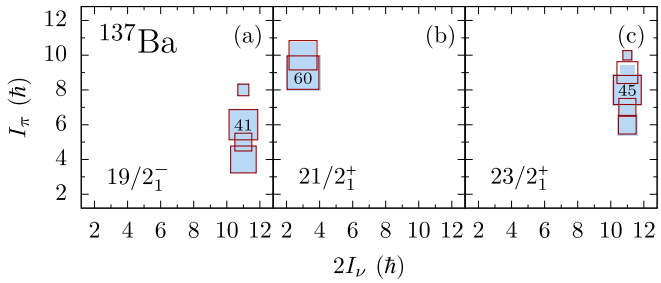

FIG. 11. Decomposition of the total angular momentum of selected states of ^{137}Ba, using the GCN50:82 interaction (filled blue boxes) and the SN100PN interaction (empty red boxes) into their proton and neutron spins $I_\pi \otimes I_\nu$.

branches into the $J^\pi = 19/2^-$ or $21/2^-$ state, they have most likely spins $J > 23/2$. By a similar argument the 3322- and 4152-keV states are interpreted to have a spin of $J > 21/2$. Otherwise, they would directly decay to the $J^\pi = 19/2^-$ state.

The theoretical wave functions of ^{137}Ba are not as fragmented as in ^{136}Ba. The decomposition of the total angular momentum $I = I_\pi \otimes I_\nu$ into its proton and neutron components for the $J^\pi = 19/2^-_1$, $21/2^+_1$, and $23/2^+_1$ states in ^{137}Ba predicted by the GCN50:82 and SN100PN is presented in Fig. 11. Table III shows the calculated average neutron occupation numbers of each orbital in the *gdsh* model space. For GCN50:82, the $J^\pi = 19/2^-_1$ isomer consists mainly (29%) of the $\nu h^{-1}_{11/2} \otimes \pi(g^5_{7/2}d^1_{5/2})$, 21% of the $\nu h^{-1}_{11/2} \otimes \pi(g^3_{7/2}d^3_{5/2})$, and 13% of the $\nu h^{-1}_{11/2} \otimes \pi(g^4_{7/2}d^2_{5/2})$ configuration. The dominating neutron-hole $\nu h^{-1}_{11/2}$ configuration is also visible in the average occupation numbers with an occupation of $N_\nu \approx 11$ in the neutron $h_{11/2}$ orbital. Also the SN100PN and the realistic-SM calculation predict a strong neutron-hole $\nu h^{-1}_{11/2}$ configuration for the $J^\pi = 19/2^-_1$ state. Couplings of this configuration to proton configurations with spins of 4^+ (33%), 5^+ (16%), and 6^+ (41%) contribute to the $J^\pi = 19/2^-_1$ state. Also for the $J^\pi = 21/2^-$, $J^\pi = 23/2^-$, and higher-lying negative-parity states the neutron $\nu h^{-1}_{11/2}$ configuration dominates.

The positive-parity bands in ^{136}Ba and ^{137}Ba have mirroring structures. In each nucleus, positive-parity bands are connected via a high-energy (≈1.2 MeV) transition to the negative-parity band. Like the $J^\pi = 12^+$ bandhead in ^{136}Ba, the $J^\pi = 21/2^+$ bandhead in ^{137}Ba shows a smaller degree of $\nu d_{3/2}$ occupation than for the $J^\pi = 19/2^-$ state. The $\nu h_{11/2}$ orbital becomes fully occupied, as calculated by GCN50:82, realistic SM, and SN100PN (see Table III). GCN50:82 predicts a mixture of (67%) $\nu d^{-1}_{3/2} \otimes \pi(g^5_{7/2}d^1_{5/2})$ and (11%) $\nu d^{-1}_{3/2} \otimes \pi(g^3_{7/2}d^3_{5/2})$ with dominating proton-spin components of $I_\pi = 9^+$ and 10^+ coupled to neutron spin $I_\nu = 3/2^+$ in the $J^\pi = 21/2^+$ state in ^{137}Ba. All three interactions predict a similar structure for the $J^\pi = 21/2^+$ state. From the second excited state in this band onwards ($J^\pi \geqslant 23/2^+_1$), the valence neutron hole is mainly occupying the $\nu h_{11/2}$ orbital. As a consequence a dominating neutron spin of $I_\nu = 11/2^-$ returns to prevail, as shown in Fig. 11(c). According to the distinct similarities of the configurations, the $J^\pi = 21/2^+$ bandhead in ^{137}Ba can be interpreted as the configuration of the $J^\pi = 12^+$ state in ^{136}Ba coupled to a $\nu h_{11/2}$ neutron hole. Interestingly, in ^{137}Ba SN100PN is able to describe the predominant proton character of the $J^\pi = 21/2^+$ state, which is the $J^\pi = 12^+$ state analogon in the even-even core ^{136}Ba, to which a single neutron is coupled, but it is unable to describe the proton structure of the $J^\pi = 12^+$ state in ^{136}Ba.

TABLE III. Average neutron occupation numbers in each single-particle orbit of the *gdsh* model space in ^{137}Ba, calculated using the GCN50:82 and SN100PN interaction.

J^π	$g_{7/2}$	$d_{5/2}$	$d_{3/2}$	$s_{1/2}$	$h_{11/2}$
			GCN50:82		
$19/2^-_1$	8.00	6.00	4.00	2.00	11.00
$21/2^+_1$	7.98	5.98	3.07	1.98	11.99
$23/2^+_1$	8.00	6.00	4.00	2.00	11.00
			SN100PN		
$19/2^-_1$	8.00	6.00	4.00	2.00	11.00
$21/2^+_1$	7.99	5.98	3.08	1.96	12.00
$23/2^+_1$	8.00	6.00	4.00	2.00	11.00

V. CONCLUSIONS

In summary, four experiments employing two ^{9}Be + ^{130}Te and one ^{11}B + ^{130}Te fusion-evaporation reactions as well as the ^{136}Xe + ^{238}U multinucleon-transfer reaction were used to investigate high-spin states above the $J^\pi = 10^+$ isomer in ^{136}Ba and above the $J^\pi = 19/2^-$ isomer in ^{137}Ba. The level scheme of ^{136}Ba was revised, incorporating nine new states and transitions. Proper spin and multipolarity assignments were determined by γ-ray angular distribution measurements and $\gamma\gamma$ coincidence relations. The $E_x = 4920$-keV state is identified as the $J^\pi = 12^+$ state. The high-spin regime of ^{136}Ba differs significantly from the lower mass isotones.

While the high-spin regimes of both ^{132}Te and ^{134}Xe exhibit high-energy $12^+ \rightarrow 10^+$ yrast transitions, no such transition is observed in ^{136}Ba. Instead the $J^\pi = 10^+$ isomer is fed by a $J^\pi = 11^-$ state. This disruption in the nuclear structure along the $N = 80$ isotones is explained by a dominant proton configuration of the $J^\pi = 12^+$ state in ^{136}Ba. While the $J^\pi = 10^+$ isomer consists mainly of neutron configurations, a pure proton configuration for the $J^\pi = 12^+$ state and the interrupting $J^\pi = 11^-$ state is energetically favorable compared to the continuation via a $\nu h_{11/2}$ configuration. The configuration of the $J^\pi = 12^+$ state mirrors the structure of the $J^\pi = 8^+$ state below the isomer. ^{136}Ba is the first isotone along $N = 80$ for which a combined proton alignment in the $g_{7/2}$ and $d_{5/2}$ orbitals can form a spin of $J = 12$. Corresponding shell-model calculations yield ambiguous results. Only the SN100PN interaction predicts a predominant neutron character of the $J^\pi = 12^+$ state, while GCN50:82 and realistic SM exhibit the emerging proton configuration. In previous publications, it was found that the proton-neutron part of the SN100PN interaction falls short to reproduce

several nuclear-structure features in the mass region. SN100PN could not reproduce backbending in the high-spin regime of ^{131}Xe [70] and the decay features of isomeric states in ^{135}Xe and ^{137}Ba [20]. Similar conclusions on the monopole part were also discussed in Ref. [71]. In the present study, it is worthy of attention that only interactions with improved and corrected monopole parts, i.e., GCN50:82 and realistic SM, reproduce the nonobservation of the $12^+ \rightarrow 10^+$ transition by the different structure of these two levels.

In ^{137}Ba spins above the $J^\pi = 19/2^-$ isomer at $E_x = 2350$ keV were measured for the first time. The $E_x = 3545$-keV state is proposed to be the bandhead of the positive-parity band, which is explained as the coupling of the aforementioned $J^\pi = 12^+$ state of the even-even core ^{136}Ba and a neutron. The identification of the high-spin structures complete the systematics for $N = 80$ and $N = 81$ isotones in the vicinity of the $N = 82$ shell closure. In future, measurements of lifetimes and g factors that serve as sensitive probes for nucleon alignment should be performed to independently confirm the proposed proton character of the positive-parity bandheads in ^{136}Ba and ^{137}Ba.

ACKNOWLEDGMENTS

We thank the IKP FN Tandem accelerator team for the support during the experiment. Furthermore, we express our thanks to Dr. E. Teruya and Dr. N. Yoshinaga from Saitama University, Japan, for providing the results of their shell-model calculation with the PQM130 interaction. The research leading to these results has received funding from the German BMBF under Contracts No. 05P15PKFN9 TP1 and No. 05P18PKFN9 TP1, from the European Union Seventh Framework Programme FP7/2007-2013 under Grant Agreement No. 262010 - ENSAR, from the Spanish Ministerio de Ciencia e Innovación under Contract No. FPA2011-29854-C04, from the Spanish Ministerio de Economía y Competitividad under Contract No. FPA2014-57196-C5, and from the UK Science and Technology Facilities Council (STFC). L.K. and A.V. thank the Bonn-Cologne Graduate School of Physics and Astronomy (BCGS) for financial support. One of the authors (A. Gadea) has been supported by the Generalitat Valenciana, Spain, under Grant No. PROMETEOII/2014/019, and EU under the FEDER program.

[1] B. Fogelberg, K. Heyde, and J. Sau, Energy levels and transition probabilities in ^{130}Sn, Nucl. Phys. A **352**, 157 (1981).

[2] J. Genevey, J. A. Pinston, C. Foin, M. Rejmund, R. F. Casten, H. Faust, and S. Oberstedt, Conversion electron measurements of isomeric transitions in ^{130,132}Te and ^{134}Xe, Phys. Rev. C **63**, 054315 (2001).

[3] J. J. Valiente-Dobón, P. H. Regan, C. Wheldon, C. Y. Wu, N. Yoshinaga, K. Higashiyama, J. F. Smith, D. Cline, R. S. Chakrawarthy, R. Chapman, M. Cromaz, P. Fallon, S. J. Freeman, A. Görgen, W. Gelletly, A. Hayes, H. Hua, S. D. Langdown, I. Y. Lee, X. Liang *et al.*, ^{136}Ba studied via deep-inelastic collisions: Identification of the $(\nu h_{11/2})^{-2}_{10+}$ isomer, Phys. Rev. C **69**, 024316 (2004).

[4] J. Ludziejewski, J. Bialkowski, Z. Haratym, L.-E. de Geer, A. Kerek, and J. Kozyczkowski, The life-time measurements of some high-spin states in the ^{138,139}Ce and ^{141,142}Nd nuclei, Phys. Scr. **14**, 133 (1976).

[5] J. C. Merdinger, F. A. Beck, E. Bozek, T. Byrski, C. Gehringer, Y. Schutz, and J. P. Vivien, Magnetic moments of the $I^\pi = 10^+$ isomers in Ce and Nd $N = 80$ isotones, Nucl. Phys. A **346**, 281 (1980).

[6] M. Lach, J. Styczen, R. Julin, M. Piiparinen, H. Beuscher, P. Kleinheinz, and J. Blomqvist, The 10^+ states of $\nu h^{-2}_{11/2}$ and $\pi h^2_{11/2}$ character in the $N = 80$ isotones ^{144}Gd and ^{142}Sm, Z. Phys. A **319**, 235 (1984).

[7] H. A. Roth, S. E. Arnell, D. Foltescu, Ö. Skeppstedt, J. Blomqvist, G. de Angelis, D. Bazzacco, and S. Lunardi, Yrast level structure of the neutron-deficient $N = 80$ isotones ^{146}Dy, ^{147}Ho and ^{148}Er up to high-spin values, Eur. Phys. J. A **10**, 275 (2001).

[8] S. Biswas, R. Palit, A. Navin, M. Rejmund, A. Bisoi, M. S. Sarkar, S. Sarkar, S. Bhattacharyya, D. C. Biswas, M. Caamaño, M. P. Carpenter, D. Choudhury, E. Clément, L. S. Danu, O. Delaune, F. Farget, G. de France, S. S. Hota, B. Jacquot, A. Lemasson *et al.*, Structure of $^{132}_{52}$Te$_{80}$: The two-particle and two-hole spectrum of $^{132}_{50}$Sn$_{82}$, Phys. Rev. C **93**, 034324 (2016).

[9] A. Vogt, B. Birkenbach, P. Reiter, A. Blazhev, M. Siciliano, J. J. Valiente-Dobón, C. Wheldon, D. Bazzacco, M. Bowry, A. Bracco, B. Bruyneel, R. S. Chakrawarthy, R. Chapman, D. Cline, L. Corradi, F. C. L. Crespi, M. Cromaz, G. de Angelis, J. Eberth, P. Fallon *et al.*, High-spin structure of ^{134}Xe, Phys. Rev. C **93**, 054325 (2016).

[10] P. J. Rothschild, A. M. Baxter, S. M. Burnett, M. P. Fewell, G. J. Gyapong, and R. H. Spear, Quadrupole moment of the first excited state of ^{136}Ba, Phys. Rev. C **34**, 732 (1986).

[11] M. Ohshima, S. Hayashibe, N. Kawamura, Y. Itoh, M. Fujioka, and T. Ishimatsu, Magnetic moment of the 2140.2 kev 5^- state in ^{136}Ba, Hyperfine Interact. **7**, 103 (1979).

[12] W. Gelletly, J. A. Moragues, M. A. J. Mariscotti, and W. R. Kane, ^{135}Ba(n,γ) reaction and level structure of ^{136}Ba, Phys. Rev. **181**, 1682 (1969).

[13] E. Dragulescu, G. Semenescu, and I. Iftimia, Nuclear structure studies of nuclei near $N = 80$, J. Phys. **53**, 447 (1999).

[14] T. Shizuma, Z. G. Gan, K. Ogawa, H. Nakada, M. Oshima, Y. Toh, T. Hayakawa, Y. Hatsukawa, M. Sugawara, Y. Utsuno, and Z. Liu, A new isomer in ^{136}Ba populated by deep inelastic collisions, Eur. Phys. J. A **20**, 207 (2004).

[15] T. Bhattacharjee, S. Chanda, S. Bhattacharyya, S. K. Basu, R. K. Bhowmik, J. J. Das, U. Datta Pramanik, S. S. Ghugre, N. Madhavan, A. Mukherjee, G. Mukherjee, S. Muralithar, and R. P. Singh, Band structures in near spherical ^{138}Ce, Nucl. Phys. A **825**, 16 (2009).

[16] C. M. Petrache, M. Fantuzi, G. LoBianco, D. Mengoni, A. Neusser-Neffgen, H. Hübel, A. Al-Khatib, P. Bringel, A. Bürger, N. Nenoff, G. Schönwasser, A. K. Singh, I. Ragnarsson, G. B. Hagemann, B. Herskind, D. R. Jensen, G. Sletten, P. Fallon, A. Görgen, P. Bednarczyk *et al.*, Evolution from spherical single-particle structure to stable triaxiality at high spins in ^{140}Nd, Phys. Rev. C **72**, 064318 (2005).

[17] E. Gülmez, H. Li, and J. A. Cizewski, Level structure of ^{140}Nd, Phys. Rev. C **36**, 2371 (1987).

[18] C. M. Petrache, R. A. Bark, S. T. H. Murray, M. Fantuzi, E. A. Lawrie, S. Lang, J. J. Lawrie, S. M. Maliage, D. Mengoni, S. M. Mullins, S. S. Ntshangase, D. Petrache, T. M. Ramashidzha, and I. Ragnarsson, Six-quasiparticle isomer in ^{140}Nd, Phys. Rev. C **74**, 034304 (2006).

[19] M. Ferraton, R. Bourgain, C. M. Petrache, D. Verney, F. Ibrahim, N. de Séréville, S. Franchoo, M. Lebois, C. Phan Viet, L. Sagui, I. Stefan, J. F. Clavelin, and M. Vilmay, Lifetime measurement of the six-quasiparticle isomer in ^{140}Nd and evidence for an isomer above the $19/2^+$ state in ^{139}Nd, Eur. Phys. J. A **35**, 167 (2008).

[20] A. Vogt, B. Birkenbach, P. Reiter, A. Blazhev, M. Siciliano, K. Hadyńska-Klęk, J. J. Valiente-Dobón, C. Wheldon, E. Teruya, N. Yoshinaga, K. Arnswald, D. Bazzacco, M. Bowry, A. Bracco, B. Bruyneel, R. S. Chakrawarthy, R. Chapman, D. Cline, L. Corradi, F. C. L Crespi *et al.*, Isomers and high-spin structures in the $N = 81$ isotones ^{135}Xe and ^{137}Ba, Phys. Rev. C **95**, 024316 (2017).

[21] A. Kerek and J. Kownacki, The level structure of the $N = 81$ and 82 nucleides ^{137,138}Ba as investigated in ^{136}Xe(α, xn) reactions, Nucl. Phys. A **206**, 245 (1973).

[22] Evaluated Nuclear Structure Data File (ENSDF), http://www.nndc.bnl.gov/ensdf

[23] S. Kaim, C. M. Petrache, A. Gargano, N. Itaco, T. Zerrouki, R. Leguillon, A. Astier, I. Deloncle, T. Konstantinopoulos, J. M. Régis, D. Wilmsen, B. Melon, A. Nannini, C. Ducoin, D. Guinet, and T. Bhattacharjee, High-spin spectroscopy of ^{139}Ce, Phys. Rev. C **91**, 024318 (2015).

[24] P. Bhattacharyya, P. J. Daly, C. T. Zhang, Z. W. Grabowski, S. K. Saha, B. Fornal, R. Broda, W. Urban, I. Ahmad, D. Seweryniak, I. Wiedenhöver, M. P. Carpenter, R. V. F. Janssens, T. L. Khoo, T. Lauritsen, C. J. Lister, P. Reiter, and J. Blomqvist, Yrast excitations in $n = 81$ nuclei ^{132}Sb and ^{133}Te from ^{248}Cm fission, Phys. Rev. C **64**, 054312 (2001).

[25] J. K. Hwang, A. V. Ramayya, J. H. Hamilton, C. J. Beyer, J. O. Rasmussen, Y. X. Luo, S. C. Wu, T. N. Ginter, C. M. Folden, P. Fallon, P. M. Zielinski, K. E. Gregorich, A. O. Macchiavelli, M. Stoyer, S. J. Asztalos, A. Covello, and A. Gargano, Particle-hole excited states in ^{133}Te, Phys. Rev. C **65**, 034319 (2002).

[26] Yu. Khazov, A. Rodionov, and F. G. Kondev, Nuclear data sheets for $A = 133$, Nucl. Data Sheets **112**, 855 (2011).

[27] B. K. Wagner, P. E. Garrett, Minfang Yeh, and S. W. Yates, On the first excited state of ^{137}Ba, J. Radioanal. Nucl. Chem. **219**, 217 (1997).

[28] I. Bikit, I. Aničin, J. Slivka, M. Krmar, J. Puzović, and Lj. Čonkić, Population of the 283 keV level of ^{137}Ba by the β decay of ^{137}Cs, Phys. Rev. C **54**, 3270 (1996).

[29] V. A. Bondarenko, I. L. Kuvaga, P. T. Prokofjev, A. M. Sukhovoj, V. A. Khitrov, Yu. P. Popov, S. Brant, and V. Paar, Levels of ^{137}Ba studied with neutron-induced reactions, Nucl. Phys. A **582**, 1 (1995).

[30] E. Dragulescu, M. Ivascu, R. Mihu, D. Popescu, G. Semenescu, A. Velenik, and V. Paar, Coulomb excitation of levels in ^{135}Ba and ^{137}Ba, J. Phys. G **10**, 1099 (1984).

[31] S. Chanda, T. Bhattacharjee, S. Bhattacharyya, A. Mukherjee, S. K. Basu, I. Ragnarsson, R. K. Bhowmik, S. Muralithar, R. P. Singh, S. S. Ghugre, and U. D. Pramanik, Seven-quasiparticle bands in ^{139}Ce, Phys. Rev. C **79**, 054332 (2009).

[32] D. Bucurescu, G. Căta-Danil, I. Căta-Danil, M. Ivaşcu, N. Mărginean, R. Mărginean, L. C. Mihăilescu, C. Rusu, and G. Suliman, Gamma-ray spectroscopy of the nucleus ^{139}Ce, Eur. Phys. J. A **27**, 301 (2006).

[33] S. Bhowal, C. Lahiri, R. Raut, P. Singh, M. K. Raju, A. Goswami, A. K. Singh, S. Bhattacharya, T. Bhattacharjee, G. Mukherjee *et al.*, Energy levels in ^{141}Nd from fusion evaporation study, J. Phys. G. **38**, 035105 (2011).

[34] T. Zerrouki, C. M. Petrache, R. Leguillon, K. Hauschild, A. Korichi, A. Lopez Martens, S. Frauendorf, I. Ragnarsson, H. Hübel, A. Neußer-Neffgen, A. Al-Khatib, P. Bringel, A. Bürger, N. Nenoff, G. Schönwaßer, A. K. Singh, D. Curien, G. B. Hagemann, B. Herskind, G. Sletten, P. Fallon, A. Görgen, and P. Bednarczyk, Shape evolution and magnetic rotation in ^{141}Nd, Eur. Phys. J. A **51**, 50 (2015).

[35] S. Akkoyun *et al.*, AGATA – Advanced GAmma Tracking Array, Nucl. Instrum. Methods Phys. Res., Sect. A **668**, 26 (2012).

[36] A. M. Stefanini, L. Corradi, G. Maron, A. Pisent, M. Trotta, A. M. Vinodkumar, S. Beghini, G. Montagnoli, F. Scarlassara, G. F. Segato, A. De Rosa, G. Inglima, D. Pierroutsakou, M. Romoli, M. Sandoli, G. Pollarolo, and A. Latina, The heavy-ion magnetic spectrometer PRISMA, Nucl. Phys. A **701**, 217 (2002).

[37] L. Corradi, S. Szilner, G. Pollarolo, D. Montanari, E. Fioretto, A. M. Stefanini, J. J. Valiente-Dobón, E. Farnea, C. Michelagnoli, G. Montagnoli, F. Scarlassara, C. A. Ur, T. Mijatović, D. Jelavić Malenica, N. Soić, and F. Haas, Multinucleon transfer reactions: Present status and perspectives, Nucl. Instrum. Methods Phys. Res., Sect. B **317**, 743 (2013).

[38] S. Szilner, C. A. Ur, L. Corradi, N. Marginean, G. Pollarolo, A. M. Stefanini, S. Beghini, B. R. Behera, E. Fioretto, A. Gadea, B. Guiot, A. Latina, P. Mason, G. Montagnoli, F. Scarlassara, M. Trotta, G. de Angelis, F. Della Vedova, E. Farnea, F. Haas *et al.*, Multinucleon transfer reactions in closed-shell nuclei, Phys. Rev. C **76**, 024604 (2007).

[39] L. Netterdon, V. Derya, J. Endres, C. Fransen, A. Hennig, J. Mayer, C. Müller-Gatermann, A. Sauerwein, P. Scholz, M. Spieker, and A. Zilges, The γ-ray spectrometer HORUS and its applications for nuclear astrophysics, Nucl. Instrum. Methods Phys. Res., Sect. A **754**, 94 (2014).

[40] A. Gadea, E. Farnea, J. J. Valiente-Dobón, B. Million, D. Mengoni, D. Bazzacco, F. Recchia, A. Dewald, Th. Pissulla, W. Rother, G. de Angelis *et al.*, Conceptual design and infrastructure for the installation of the first AGATA sub-array at LNL, Nucl. Instrum. Methods Phys. Res., Sect. A **654**, 88 (2011).

[41] A. Wiens, H. Hess, B. Birkenbach, B. Bruyneel, J. Eberth, D. Lersch, G. Pascovici, P. Reiter, and H.-G. Thomas, The AGATA triple cluster detector, Nucl. Instrum. Methods Phys. Res., Sect. A **618**, 223 (2010).

[42] B. Bruyneel, B. Birkenbach, and P. Reiter, Pulse shape analysis and position determination in segmented HPGe detectors: The AGATA detector library, Eur. Phys. J. A **52**, 70 (2016).

[43] A. Lopez-Martens, K. Hauschild, A. Korichi, J. Roccaz, and J.-P. Thibaud, γ-ray tracking algorithms: a comparison, Nucl. Instrum. Methods Phys. Res., Sect. A **533**, 454 (2004).

[44] A. Vogt, B. Birkenbach, P. Reiter, L. Corradi, T. Mijatović, D. Montanari, S. Szilner, D. Bazzacco, M. Bowry, A. Bracco, B. Bruyneel, F. C. L. Crespi, G. de Angelis, P. Désesquelles, J. Eberth, E. Farnea, E. Fioretto, A. Gadea, K. Geibel, A.

Gengelbach *et al.*, Light and heavy transfer products in ^{136}Xe + ^{238}U multinucleon transfer reactions, Phys. Rev. C **92**, 024619 (2015).

[45] N. Saed-Samii, Lifetime measurements using the FATIMA array in combination with EXOGAM@ILL, Diplomarbeit, Universität zu Köln (unpublished).

[46] J. Theuerkauf, Die Analyse von zwei- und mehrdimensionalen $\gamma\gamma$-Koinzidenzspektren an Beispielen aus Hochspinexperimenten in der Massengegend um ^{146}Gd, Ph.D. thesis, Universität zu Köln, 1994.

[47] I. Wiedenhöver, computer code CORLEONE, 1997.

[48] I. Wiedenhöver, O. Vogel, H. Klein, A. Dewald, P. von Brentano, J. Gableske, R. Krücken, N. Nicolay, A. Gelberg, P. Petkov, A. Gizon, J. Gizon, D. Bazzaco, C. Rossi Alvarez, G. de Angelis, S. Lunardi, P. Pavan, D. R. Napoli, S. Frauendorf, F. Dönau, R. V. F. Janssens, and M. P. Carpenter, Detailed angular correlation analysis with 4π spectrometers: Spin determinations and multipolarity mixing measurements in ^{128}Ba, Phys. Rev. C **58**, 721 (1998).

[49] K. S. Krane and R. M. Steffen, Determination of the $E2/M1$ Multipole Mixing Ratios of the Gamma Transitions in ^{110}Cd, Phys. Rev. C **2**, 724 (1970).

[50] K. S. Krane, R. M. Steffen, and R. M. Wheeler, Directional correlations of gamma radiations emitted from nuclear states oriented by nuclear reactions or cryogenic methods, At. Data Nucl. Data Tables **11**, 351 (1973).

[51] A. Linnemann, Das HORUS-Würfelspektrometer und Multiphononanregungen in ^{106}Cd, Ph.D. thesis, Universität zu Köln, 2006.

[52] L. Bettermann, C. Fransen, S. Heinze, J. Jolie, A. Linnemann, D. Mücher, W. Rother, T. Ahn, A. Costin, N. Pietralla, and Y. Luo, Candidates for the one-phonon mixed-symmetry state in ^{130}Xe, Phys. Rev. C **79**, 034315 (2009).

[53] S. Kumar, A. K. Jain, Alpana Goel, S. S. Malik, R. Palit, H. C. Jain, I. Mazumdar, P. K. Joshi, Z. Naik, A. Dhal, T. Trivedi, I. Mehrotra, S. Appannababu, L. Chaturvedi, V. Kumar, R. Kumar, D. Negi, R. P. Singh, S. Muralithar, R. K. Bhowmik, and S. C. Pancholi, Band structure and shape coexistence in $^{135}_{56}$Ba$_{79}$, Phys. Rev. C **81**, 067304 (2010).

[54] S. Chanda, T. Bhattacharjee, S. Bhattacharyya, S. K. Basu, R. K. Bhowmik, S. Muralithar, R.P. Singh, B. Mukherjee, N. S. Pattabiraman, S. S. Ghugre, and M. B. Chatterjee, High spin spectroscopy of ^{137}La, Nucl Phys. A **775**, 153 (2006).

[55] T. Yamazaki, Tables of coefficients for angular distribution of gamma rays from aligned nuclei, Nucl. Data, Sect. A **3**, 1 (1967).

[56] Y. Khazov, A. A. Roionpv, S. Sakharov, and B. Singh, Nuclear data sheets for $A = 132$, Nucl. Data Sheets **104**, 497 (2005).

[57] M. Kortelahti, A. Pakkanen, M. Piiparinen, T. Komppa, and R. Komu, Medium-spin levels and a 360 ns $I^{\pi} = 19/2^{-}$ isomer in the $N = 80$ nucleus ^{137}La, Nucl. Phys. A **376**, 1 (1982).

[58] B. A. Brown and W. D. M. Rae, The Shell-Model Code NuShellX@MSU, Nucl. Data Sheets **120**, 115 (2014).

[59] N. Shimizu, Nuclear shell-model code for massive parallel computation, "KSHELL", arXiv:1310.5431.

[60] E. Caurier, G. Martínez-Pinedo, F. Nowacki, A. Poves, and A. P. Zuker, The shell model as a unified view of nuclear structure, Rev. Mod. Phys. **77**, 427 (2005).

[61] E. Caurier, F. Nowacki, A. Poves, and K. Sieja, Collectivity in the light xenon isotopes: A shell model study, Phys. Rev. C **82**, 064304 (2010).

[62] E. Caurier, F. Nowacki, and A. Poves, Shell Model description of the $\beta\beta$ decay of ^{136}Xe, Phys. Lett. B **711**, 62 (2012).

[63] R. Machleidt, F. Sammarruca, and Y. Song, Nonlocal nature of the nuclear force and its impact on nuclear structure, Phys. Rev. C **53**, R1483 (1996).

[64] L. Coraggio, A. Covello, A. Gargano, N. Itaco, and T. T. S. Kuo, Effective shell-model hamiltonians from realistic nucleon-nucleon potentials within a perturbative approach, Ann. Phys. **327**, 2125 (2012).

[65] L. Coraggio, A. Covello, A. Gargano, N. Itaco, and T. T. S. Kuo, Shell-model calculations and realistic effective interactions, Prog. Part. Nucl. Phys. **62**, 135 (2009).

[66] L. Coraggio, L. De Angelis, T. Fukui, A. Gargano, and N. Itaco, Calculation of gamow-teller and two-neutrino double-β decay properties for ^{130}Te and ^{136}Xe with a realistic nucleon-nucleon potential, Phys. Rev. C **95**, 064324 (2017).

[67] E. Teruya, N. Yoshinaga, K. Higashiyama, and A. Odahara, Shell-model calculations of nuclei around mass 130, Phys. Rev. C **92**, 034320 (2015).

[68] K. Higashiyama and N. Yoshinaga, Pair-truncated shell-model analysis of nuclei around mass 130, Phys. Rev. C **83**, 034321 (2011).

[69] B. A. Brown, N. J. Stone, J. R. Stone, I. S. Towner, and M. Hjorth-Jensen, Magnetic moments of the 2^{+}_{1} states around ^{132}Sn, Phys. Rev. C **71**, 044317 (2005).

[70] L. Kaya, A. Vogt, P. Reiter, M. Siciliano, B. Birkenbach, A. Blazhev, L. Coraggio, E. Teruya, N. Yoshinaga, K. Higashiyama, K. Arnswald, D. Bazzacco, A. Bracco, B. Bruyneel, L. Corradi, F. C. L. Crespi, G. de Angelis, J. Eberth, E. Farnea, E. Fioretto *et al.*, High-spin structure in the transitional nucleus ^{131}Xe: Competitive neutron and proton alignment in the vicinity of the $N = 82$ shell closure, Phys. Rev. C **98**, 014309 (2018).

[71] Y. Utsuno, T. Otsuka, N. Shimizu, M. Honma, T. Mizusaki, Y. Tsunoda, and T. Abe, Recent shell-model results for exotic nuclei, EPJ Web Conf. **66**, 02106 (2014).